

# Characteristic scales during the onset of radiatively driven convection: linear analysis and simulations

Yun Chang<sup>1,2</sup>† and Alberto Scotti<sup>2,3</sup>

<sup>1</sup>Department of Physical Oceanography, Woods Hole Oceanographic Institution, Woods Hole, MA, 02543, USA

<sup>2</sup>Department of Marine Sciences, The University of North Carolina at Chapel Hill, NC, 27514, USA

<sup>3</sup>School for Engineering of Matter, Transport and Energy, Arizona State University, AZ, 85287, USA

(Received xx; revised xx; accepted xx)

This paper considers the initial stage of Radiatively Driven Convection (RDC), when the perturbations from a quiescent but time-dependent background state are small. Radiation intensity is assumed to decay exponentially away from the surface, and we consider parameter regimes in which the depth of the water is greater than the decay scale of  $e$  of the radiation intensity. Both time-independent and time-periodic radiation are considered. In both cases, the background temperature profile of the water column is time-dependent. A linear analysis of the system is performed based on these time-dependent profiles. We find that the perturbations grow in time according to  $\exp[(\sigma(t)t)]$ , where  $\sigma(t)$  is a time-dependent growth rate. An appropriately defined Reynolds number is the primary dimensionless number characterising the system, determining the wavelength, vertical structure, and growth rate of the perturbations. Simulations using a Boussinesq model (the Stratified Ocean Model with Adaptive Refinement) confirm the linear analysis.

## 1. Introduction

This paper focusses on radiatively driven convection (RDC), which occurs when heat is applied to a fluid by absorption of radiation penetrating a finite distance from a boundary. To achieve convection, the resulting heating must result in an unstable buoyancy distribution developing in the fluid. In fluids where the buoyancy increases with temperature, the radiation must be applied from below. This occurs, for example, in the interior of stars, where the radiation from the inner core drives convection in the outer layer (Spiegel 1971). Conversely, in fluids where buoyancy decreases with temperature, such as fresh water below the temperature of maximum density, RDC requires that radiation be applied from above. An example of the latter in a geophysical setting occurs in temperate lakes during spring when the water column is below the critical temperature and solar radiation heats the surface layer (see e.g. Bouffard et al. 2019; Cannon et al. 2019; Austin et al. 2022). An important difference between RDC in the interior of stars and RDC in lakes is that in the former, the horizontally (or ensemble) averaged temperature profile can be assumed to be in a statistically steady state, that is, the amount of heat received from the inner core is eventually transferred to the surface and lost to space, whereas in the case of RDC in lakes heat continuously accumulates in the system. Austin et al. (2022) shows that some heat loss occurs during nighttime, but it is small compared to the net daytime heat input. Thus, the averaged temperature never achieves steady state. Additionally, and just as important, in lakes the radiation intensity is itself time-dependent, following a diurnal cycle.

RDC as it applies to temperate lakes has been the subject of several recent observational studies that focus on vertical velocity (Bogdanov et al. 2019; Bouffard et al. 2019; Cannon et al. 2019) and the scale of convection cells (Forrest et al. 2008; Yang et al. 2017; Bogdanov et al. 2019; Austin 2019; Austin et al. 2022).

These studies show that in RDC systems that are driven by a cyclical radiation which spends a significant amount in the "off" state each cycle follows a consistent pattern:

(i) Onset: the beginning of each cycle starts from a relatively quiescent state.

(ii) Linear phase: warming of the water column develops a top-heavy buoyancy distribution on which perturbations grow. In this stage, the effect of perturbations on the averaged buoyancy field is negligible. The latter is still driven solely by the absorbed radiation.

(iii) Non-linear phase: the amplitude of perturbations saturates due to nonlinear interactions.

† Email address for correspondence: yun.chang@whoi.edu

<sup>49</sup> (iv) Recovery phase: As the intensity of the radiation wanes, turbulent fluctuations decrease in intensity, <sup>50</sup> and eventually the system relaxes to a mostly quiescent state with little or no residual stratification.

<sup>51</sup> Early studies (Mironov and Terzhevik 2000; Mironov et al. 2001) suggest that if the depth is hori-<sup>52</sup> zontally uniform, when turbulence develops, the vertical divergence of the total heat flux (the sum of <sup>53</sup> turbulent and radiative heat fluxes) becomes constant with depth, that is, the rate of heating becomes <sup>54</sup> uniform, or, which is the same, the stratification profile becomes frozen in time (even as the fluid heats <sup>55</sup> up). This suggests that the stratification during the nonlinear phase is determined by the length of the <sup>56</sup> linear phase, since the stratification ceases to grow once turbulence sets in. Since advection operates on <sup>57</sup> the averaged vertical temperature gradient, whose temperature contrast at the end of the linear phase <sup>58</sup> is proportional to the time lapsed since the onset of radiation, the latter also gives an estimate for the <sup>59</sup> temperature fluctuations, at least until the waning solar radiation alters the balance and turbulence <sup>60</sup> starts eroding the temperature gradient. From this point of view, the linear phase sets the characteristics <sup>61</sup> of the turbulent phase. This provides the motivation for the present study.

<sup>62</sup> Motivated by observations of RDC in Lake Superior, Christopher et al. (2023) recently studied the <sup>63</sup> onset of RDC by applying a time-periodic heat flux to the surface of a fluid. Applying Floquet theory, <sup>64</sup> they calculated the critical Rayleigh number and normalised wavenumber as a function of normalised <sup>65</sup> frequency of thermal forcing (their figures 2 and 3), and showed that the critical Rayleigh number <sup>66</sup> captures stability properties in two-dimensional numerical simulations (their figures 8 and 9).

<sup>67</sup> Although appropriate to consider the stability of the background RDC state, the analysis in Christo-<sup>68</sup> pher et al. cannot be used to study the evolution of perturbations at geophysical scales. The maximum <sup>69</sup> normalised frequency considered in Christopher et al. (2023) is 100, while, for example, the normalised <sup>70</sup> frequency in geophysical settings such as Lake Superior is of  $O(10^7)$ . Moreover, their analysis does not <sup>71</sup> provide the growth rate and vertical structure of the most unstable mode, nor are any characteristics of <sup>72</sup> the system described when the Rayleigh number exceeds the critical value.

<sup>73</sup> Christopher et al.'s analysis applies to cases where the time scale of evolution of the perturbations <sup>74</sup> is comparable to or larger than the period of the forcing, but at more geophysically relevant scales the <sup>75</sup> perturbations grow on a time scale much shorter than the forcing period.

<sup>76</sup> Yet, the onset is still followed by a period in time during which the perturbations are still small, so <sup>77</sup> a linearised treatment is still appropriate. With this in mind, here we develop a theory that applies to <sup>78</sup> systems in which appropriately defined Reynolds and Péclet numbers are large, and the forcing can be <sup>79</sup> time-dependent. This is not intended to provide a stability analysis of RDC in the traditional sense. <sup>80</sup> The aim of the latter is to determine over which range of values of the relevant parameters the system <sup>81</sup> develops instabilities. In our analysis, we consider the linearised regime in the limit of large Reynolds <sup>82</sup> numbers, where we expect the system to be unstable, and we concentrate on two questions:

- <sup>83</sup> 1. What are the wavelength, vertical structure, and growth rate of the growing perturbations during the <sup>84</sup> initial linear growth stage for RDC driven at geophysical scales?
- <sup>85</sup> 2. How do these features relate to environmental parameters such as radiation intensity and penetration <sup>86</sup> depth?

<sup>87</sup> We consider the problem from the point of view of an initial-value problem. At  $t = 0$  radiation is <sup>88</sup> applied to the surface of a motionless, unstratified fluid with a realistic e-folding decay scale, where the <sup>89</sup> radiation can be either time-independent or can have a diurnal cycle, and we follow the growth of a <sup>90</sup> perturbation from  $t = 0$  driven by the time-evolving background state.

<sup>91</sup> We find that perturbations do not follow the typical exponential growth  $\exp(\alpha t)$ , which may be <sup>92</sup> expected for instabilities that grow on an otherwise constant-in-time background, ( $\alpha$  being the constant <sup>93</sup> in-time growth rate). Instead, the perturbations grow as  $\exp[(\sigma(t)t)]$  and  $\sigma(t) \propto t^{n/2}$  with  $n = 1$  for <sup>94</sup> time-<sup>95</sup> independent radiation and  $n = 2$  for time-periodic radiation (the latter for times shorter than the <sup>96</sup> period).

<sup>96</sup> This paper is organised as follows. In Section 2 we linearise the equations of motions by considering <sup>97</sup> a time-varying basic state buoyancy profile which is heated by radiative forcing, whose evolution is <sup>98</sup> considered in Section 3; in Section 4 we estimate scalings for velocity and buoyancy by balancing the <sup>99</sup> dominant terms in perturbation equations and introduce the relevant nondimensional parameters; in <sup>100</sup> Section 5 we explore the behaviour of the perturbations under linearised dynamics in the limit of large <sup>101</sup> Reynolds number; in Section 6 we use Direction Numerical Simulations (DNS) to confirm the prediction <sup>102</sup> obtained from the linearised equations; finally we provide a summary and conclusions. Several Appendices <sup>103</sup> discuss technical points.

104 2. R D C in the linearised regime

105 We consider a fluid with a linear equation of state for the density  $\rho = \rho_0(1 - \alpha T)$ , where  $T$  is the  
 106 temperature. We assume a negative thermal expansion coefficient  $\alpha$ . The fluid is subject to a radiative 107  
 forcing applied to the surface. The applied heat flux  $S_0 e^{z/Z_0} F(t)$  decays exponentially away from the 108  
 surface and can be modulated in time (figure 1). The problem under the Boussinesq approximation can 109 be  
 formulated as follows

$$110 \quad \frac{D\tilde{u}}{Dt} = -\frac{1}{\rho_0} \tilde{p} + b\tilde{e}_3 + v\tilde{\nabla}^2 \tilde{u}, \quad \tilde{\nabla} \cdot \tilde{u} = 0, \quad (2.1)$$

$$111 \quad \frac{D\tilde{b}}{Dt} = -\frac{B}{Z_0} F(t) e^{\frac{z}{Z_0}} + \kappa \tilde{\nabla}^2 \tilde{b}. \quad (2.2)$$

112 Here  $\tilde{u} = (\tilde{u}, \tilde{v}, \tilde{w})$  is the velocity,  $\tilde{p}$  is the pressure deviation from the hydrostatic profile,  $b \tilde{=} g(\rho_0 - 113 \rho)/\rho_0 = \alpha g T$  is the buoyancy,  $B = (-\alpha g S_0 / \rho_0 C_p)$  is the buoyancy flux due to the radiative heat flux 114  
 $S_0$ ,  $\rho_0$  is the reference density,  $C_p$  is the heat capacity,  $g$  is the gravitational acceleration,  $Z_0$  is the 115  
 e-folding decay scale of the radiation flux,  $v$  is the molecular viscosity,  $\kappa$  is the molecular heat diffusivity, 116 and  
 $e_3$  is the unit vector pointing upward. The surface through which radiation is applied is at  $z = 0$  117 and the  
 domain extends below to  $z = -H$ . All thermodynamic quantities are evaluated at the reference 118  
 temperature. Mutatis mutandis, the same configuration applies to radiation applied to the bottom of a 119  
 fluid with a positive expansion coefficient, with the understanding that in this case  $Z_0 < 0$ .

119 For time-independent radiation,

$$120 \quad F(t) = 1, \quad (2.3)$$

120 while for diurnal solar radiation

$$121 \quad F(t) = \sin(\Omega t) \quad \text{if } t < \tau_{DTL}, \quad \text{else } 0, \quad (2.4)$$

122 where  $\Omega = \pi/\tau_{DTL}$  and  $\tau_{DTL}$  is the daytime length.

122 We decompose the motion into a basic state and perturbations

$$123 \quad \tilde{u} = 0 + u(x, t), \quad \tilde{b} = \bar{b}(z, t) + b(x, t), \quad \tilde{p} = \bar{p} + p(x, t). \quad (2.5)$$

123 Here  $x = (x, y, z)$  and  $\bar{b}(z, t = 0) = 0$ . The basic state satisfies

$$124 \quad 0 = -\frac{1}{\rho_0} \bar{p} + b\bar{e}_3, \quad (2.6)$$

$$125 \quad \frac{\partial \bar{b}}{\partial t} = -\frac{B}{Z_0} F(t) e^{\frac{z}{Z_0}} + \kappa \frac{\partial^2 \bar{b}}{\partial z^2}. \quad (2.7)$$

125 From here, we follow the same approach used to study the stability of Rayleigh-Bénard convection  
 126 (Chandrasekhar 1961). Subtracting the basic state momentum equation (2.6) from (2.1) and then  
 127 neglecting squares of perturbations, the linearized perturbation momentum equation reads

$$128 \quad \frac{\partial u}{\partial t} = -\frac{1}{\rho_0} \bar{p} + b\bar{e}_3 + v\tilde{\nabla}^2 u, \quad (2.8)$$

128 From (2.8) and the incompressibility condition we derive a single equation for the Laplacian of the  
 129 vertical velocity

$$130 \quad \frac{\partial \tilde{w}}{\partial t} = \tilde{\nabla}^2 \tilde{b} + v\tilde{\nabla}^2 \tilde{\nabla}^2 w. \quad (2.9)$$

130 Here,  $\tilde{\nabla}^2 = \partial^2/\partial x^2 + \partial^2/\partial y^2$  is the horizontal Laplacian operator. Subtracting the basic state buoyancy  
 131 equation (2.7) from (2.2) and then neglecting squares of perturbations, the linearized perturbation  
 132 buoyancy equation reads

$$133 \quad \frac{\partial b}{\partial t} + w \frac{\partial \bar{b}(z, t)}{\partial z} = \kappa \tilde{\nabla}^2 b. \quad (2.10)$$

133 Substituting  $\tilde{\nabla}^2 \tilde{b}$  in (2.9) into  $\tilde{\nabla}^2$  [2.10], these two equations can be combined as

$$134 \quad \frac{\partial^2 \tilde{w}}{\partial t^2} + (\tilde{\nabla}^2 \tilde{w}) \frac{\partial \bar{b}}{\partial z} - (v + \kappa) \frac{\partial}{\partial t} \tilde{\nabla}^2 \tilde{w} + v\kappa \tilde{\nabla}^2 \tilde{\nabla}^2 \tilde{w} = 0. \quad (2.11)$$

134 (2.7), (2.9) and (2.10) will be used to find scalings for the linear system. (2.11) will be used to find the  
 135 growth rate and the spatial structure of the perturbations.

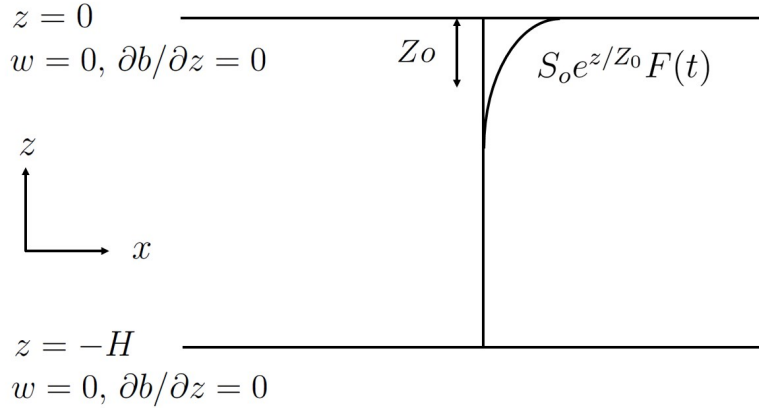


Figure 1: Schematic of RDC.

### 136 3. Evolution of the background profile

137 With an appropriate choice of a vertical velocity scale  $W_0$ , a buoyancy scale  $b_0$ , and a time scale  $t_0$  (to  
 138 be defined in the next section), we define dimensionless vertical velocity, buoyancy, time, and coordinates

$$\hat{w} = w/W_0, \quad \hat{b} = b/b_0, \quad \hat{t} = t/t_0, \quad \hat{x} = x/Z_0, \quad \hat{y} = y/Z_0, \quad \hat{z} = z/Z_0. \quad (3.1)$$

139 We also define a Reynolds number  $Re \equiv W_0 Z_0 / v$  and a Péclet number  $Pe \equiv W_0 Z_0 / k$ . From the  
 140 buoyancy scale, we can derive a temperature scale  $T_0 = b_0 / (-\alpha g)$ . In the following we will dispense from  
 141 decorating non-dimensional variables, and all variables except those in section 4 are non-dimensional.

142 The background buoyancy profile satisfies

$$\frac{\partial \bar{b}}{\partial \bar{t}} = -F(t) e^{\bar{z}} + \frac{1}{Pe} \frac{\partial^2 \bar{b}}{\partial \bar{z}^2}, \quad (3.2)$$

143 where the Péclet number  $Pe$  is the ratio of the perturbation time scale (to be defined more precisely  
 144 later) to the diffusive time scale  $Z^2/k$ . This equation needs to be solved subject to boundary and initial  
 145 conditions. For the latter, we simply choose  $b(z, 0) = 0$ . At the bottom ( $z = -H$ ) of the water column,  
 146 the natural choice is a no-flux condition. At the surface, we assume that the latent, sensible and long-  
 147 wavelength radiative heat flux are small compared to the incoming short-wave heat flux, and thus we  
 148 approximate the surface boundary condition with a no-flux condition as well. This approximation is  
 149 suggested by the observations of Austin et al. (2022) who reports that the total increase in the heat  
 150 content of the water column as a function of time can be, to a great degree of accuracy, predicted by  
 151 integrating the equation for heat over the water column with no-flux conditions at both boundaries. As  
 152 we shall see, for large values of  $Pe$ , the evolution of the perturbations is primarily controlled by the  
 153 evolution of the stratification in the bulk of the water column driven by the absorbed radiation. With  
 154 these boundary conditions, (3.2) can be solved by writing the solution as a standard trigonometric series.  
 155 The vertical gradient of the general solution is thus

$$\frac{\partial \bar{b}}{\partial \bar{z}}(z, t) = \sum_{m=1}^{\infty} a_m R(\lambda_m^2 / Pe, t) \sin(\lambda_m z), \quad (3.3)$$

156 where the wave number  $\lambda_m = m\pi/H$ , and the coefficients

$$a_m = \frac{2\lambda_m}{H} \frac{1 - (-1)^m e^{-H}}{1 + \lambda_m^2}. \quad (3.4)$$

157 The function  $R(s, t)$  describes the relaxation of the solution to the stationary state (which is not steady  
 158 for diurnal radiation)

$$R(s, t) = \begin{cases} \frac{1 - e^{-\alpha t}}{s} & \text{if } F_s(t) = 1, \text{ (Steady radiation)} \\ e^{-\frac{\alpha t}{s}} & \text{if } F_s(t) = \sin(\Omega t), \text{ (Diurnal radiation).} \end{cases} \quad (3.5)$$

159 In the case of steady radiation,  $R(s, t) = R(st, 1)t$ . For diurnal radiation this is not in general true.  
 160 However, here we are interested in perturbations that grow on a time scale much shorter than the

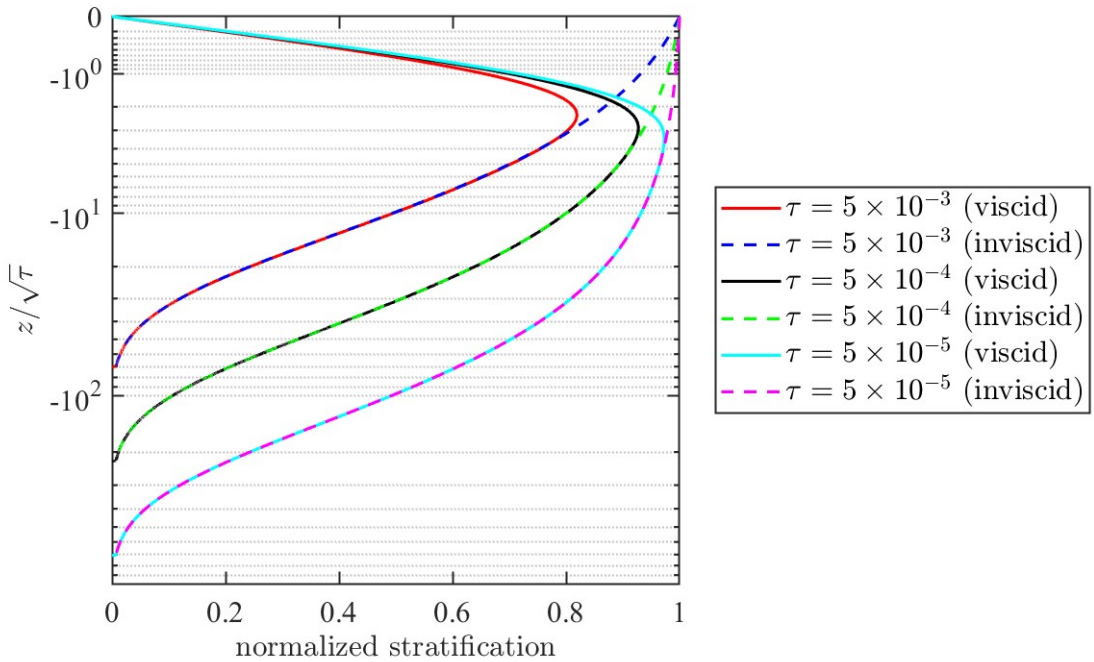


Figure 2: Profiles of  $\bar{b}/\sqrt{\tau}$  normalized with fast time (solid lines) and  $e^z$  (dashed lines) for different values of  $\tau$  plotted against  $z/\sqrt{\tau}$ . The viscous profiles depart from the inviscid solution starting at a depth which deepens as  $\sqrt{\tau}$ .

<sup>161</sup> diurnal period, i.e.  $\Omega t \gg 1$ . In this case we can approximate

$$R(s, t) \approx \Omega \frac{st - (1 - e^{-st})}{s^2} + O((\Omega t)^2), \quad (3.6)$$

<sup>162</sup> and therefore  $R(s, t) \approx R(st, 1)t^2 + O((\Omega t)^2)$ . Thus we can write a general form for the background shear

$$\frac{\partial \bar{b}}{\partial z}(z, t) = \sum_{p=1}^{\infty} a_p R(\lambda_p^2 \tau, 1) \sin(\lambda_p z) t^n \equiv S_n(z, \tau) t^n, \quad (3.7)$$

<sup>163</sup> with  $\tau = t/\Omega e$ ,  $n = 1, 2$  for steady and unsteady radiation respectively, and  $S_n(z, \tau)$  is the term in <sup>164</sup> square brackets in (3.7) with the appropriate choice for  $R$ , the relaxation function. Thus, for large values <sup>165</sup> of the Péclet number, there are two time scales that control the evolution of the background stratification <sup>166</sup> profile: the "fast" time  $t$  over which the profile evolves in a self-similar manner, and the "slow" time  $\tau$  <sup>167</sup> over which the overall shape of the profile changes as the diffusive boundary layer grows at the surface. <sup>168</sup> In particular, the inviscid solution

$$\bar{b}(z, t) = -e^z \int_0^{Z/\tau} F(t') dt'. \quad (3.8)$$

<sup>169</sup> is recovered in the limit  $\tau \rightarrow 0$ .

<sup>170</sup> For finite, but small values of  $\tau$  the inviscid solution approximates well the actual solution except <sup>171</sup> for the surface boundary layer whose thickness grows as <sup>172</sup>  $\sqrt{\tau}$  (figure 2). Of course, for this to work, <sup>173</sup> the penetration depth (which in our units is 1) must be much larger than the thickness of the surface <sup>174</sup> boundary layer during the time over which the analysis is carried. In practise, this limits the analysis <sup>175</sup> to times shorter than  $Z^2/\kappa$ . Thus, our analysis cannot be applied to Rayleigh-Benard convection driven <sup>176</sup> by a time-dependent surface heat flux (SHF convection), because that would require taking the  $Z_0 \rightarrow 0$  <sup>177</sup> limit. Physically, in time-dependent SHF the driving signal is carried into the fluid by the developing <sup>178</sup> boundary layer itself. Whereas in RDC we have a non-trivial inviscid solution which is modified over <sup>179</sup> a slow time by diffusion effects, in SHF convection the inviscid solution is trivial, and the background <sup>179</sup> system evolves under the slow time alone.

#### 180 4. Scaling and normalisation

181 In this section, we temporarily revert to dimensional quantities. There are two length scales in RDC:  
 182 the depth of water  $H$  and the radiation penetration scale  $Z_0$ . As near-surface water warms gradually and  
 183 just starts to sink, the depth of water during the initial stages of RDC should not play a role provided  
 184  $H/Z_0 \ll 1$ . Thus  $Z_0$  is the natural length scale during the onset of this process .

185 The basic state is the time-dependent solution to (2.7) given by (3.7). Clearly, both  $\bar{b}$  and  $\partial\bar{b}/\partial z$  change  
 186 continuously over time. Thus, perturbations grow against a background state which is itself changing.

187 We derive scales by balancing the dominant terms in (2.9) and (2.10). Since growing perturbations are  
 188 forced by the basic state, which is time dependent in RDC, time-derivative terms must be retained. In  
 189 the vertical momentum equation (2.9), we assume the local vertical acceleration and buoyancy balance

$$\frac{\partial \bar{w}}{\partial t} \ll \frac{\partial \bar{b}}{\partial H} \bar{b}^2. \quad (4.1)$$

190 In the buoyancy equation (2.10), we assume a balance between the local rate of increase in buoyancy  
 191 and vertical advection of buoyancy

$$\frac{\partial b}{\partial t} \ll w \frac{\partial \bar{b}(z, t)}{\partial z}. \quad (4.2)$$

192 Three equations suffice to solve for the vertical velocity scale  $W_0$ , the buoyancy scale  $b_0$ , and the time  
 193 scale  $t_0$ .

##### 194 4.1. Time independent radiation

195 The inviscid solution for the background buoyancy provides a scale for the buoyancy

$$b_0 = \frac{B}{Z_0} t_0, \quad (4.3)$$

196 which in conjunction with (4.1) and (4.2) allows us to determine the other scales

$$W_0 = (BZ_0)^{1/3}, \quad \frac{B^{1/3} b_0}{Z_0}, \quad t_0 = \frac{Z_0^{2/3}}{B}. \quad (4.4)$$

197 Substituting (3.1) and (4.4) into (2.11) we have

$$\frac{\partial^2 \bar{w}}{\partial t^2} - \bar{w}_{\text{H}} w S_1(z, \tau) t - \text{Re} \frac{1}{t} \text{Pe} \frac{1}{\partial t} \frac{\partial^2 \bar{w}}{\partial z^2} + \text{Re} \text{Pe} \frac{\partial^2 \bar{w}}{\partial z^2} = 0. \quad (4.5)$$

198 The physical interpretation of the characteristic scales (4.4) is that as the RDC develops, the perturbations grow to  $O(W_0)$  and  $O(b_0)$  over a time  $O(t_0)$ , after which the system becomes nonlinear.

200 Also, note that  $W_0 = (BZ_0)^{1/3}$  in (4.4) has the same form as the Deardorff (1970) scaling  $W^2 = (B^2 H)^{1/3}$ , which characterises the vertical velocity in SHF convection ( $B^2$  is the buoyancy flux applied to the surface and  $H$  is the depth of the water). However, the fact that the two scalings are of the same form should be viewed as a coincidence, because the two problems differ fundamentally. The Deardorff scaling characterises vertical velocity in SHF convection in the nonlinear steady state stage, while (4.4) are scalings for the linear, time-dependent stage of RDC in which the radiation profile penetrates into fluid with an e-folding decay scale  $Z_0$ .

##### 207 4.2. Diurnal solar radiation

208 In this case, the inviscid solution indicates that

$$b_0 = \frac{B}{Z_0} \Omega t_0^2. \quad (4.6)$$

209 Substituting  $W_0$ ,  $b_0$ , and  $t_0$  into (4.1), (4.2), (4.6), we have

$$\frac{W_0}{t_0} = b_0, \quad \frac{1}{t_0} = \frac{W_0}{Z_0}, \quad b_0 = \frac{B}{Z_0} \Omega t_0^2, \quad (4.7)$$

210 which together yield

$$W_0 = (B\Omega Z_0^2)^{1/4}, \quad b_0 = (B\Omega)^{1/2}, \quad t_0 = \frac{Z_0^{2/4}}{B\Omega}, \quad (4.8)$$

211 which are to be interpreted as their counterpart in the steady radiation case. Substituting (3.1) and (4.8)

212 into (2.11) and working under the assumption that  $\Omega t_0 \ll 1$  so that the background solution retains the  
213 self similar profile in the fast time  $t$ , we have

$$\frac{\partial^2 \frac{\partial^2 w}{\partial t^2}}{\partial z^2} - \frac{1}{H} w S_2(z, \tau) t^2 - \frac{1}{Re} \frac{1}{Pe} \frac{\partial^2 \frac{\partial^2 w}{\partial t^2}}{\partial z^2} + \frac{1}{Re Pe} \frac{\partial^2 \frac{\partial^2 w}{\partial t^2}}{\partial z^2} = 0. \quad (4.9)$$

## 214 5. Evolution of perturbations

215 The equations for the evolution of the perturbation under steady and periodic radiation conditions  
216 can be condensed in a single equation which in non dimensional form reads

$$\frac{\partial}{\partial t} + \frac{1}{Pe} \frac{\partial}{\partial \tau} - \frac{1}{Re} \frac{\partial^2}{\partial z^2} \frac{\partial}{\partial t} + \frac{1}{Pe} \frac{\partial}{\partial \tau} - \frac{1}{Pe} \frac{\partial^2}{\partial z^2} \frac{\partial^2 w}{\partial t^2} = S_n(z, \tau) t^n \frac{\partial^2 w}{\partial z^2}, \quad (5.1)$$

217 with  $n = 1$  describing the steady radiation case and  $n = 2$  the diurnal cycle. This equation describes the  
218 evolution of the perturbed vertical velocity  $w(x, y, z, t, \tau)$ .

219 In the geophysical settings of interest, the Reynolds and Péclet numbers are large, though not infinite,  
220 and therefore it is of consequence to consider whether (5.1) can be further simplified. To this extent, it  
221 would be tempting to discard altogether the terms proportional to  $Re^{-1}$  and  $Pe^{-1}$ . However, this would  
222 not be appropriate, since, on physical grounds, we expect that viscosity and diffusivity at sufficiently  
223 small scales cannot be ignored. However, it is reasonable to expect that no high-frequency oscillations  
224 should be expected in  $\tau$  (otherwise it would be a fast time), and thus we can neglect the term  $Pe^{-1} \partial / \partial \tau$ .  
225 Equation (5.1) is invariant under rotations around the vertical axis. Thus, we consider perturbations  
226 confined to a two-dimensional vertical plane. Since equation (5.1) is not homogeneous in fast time, the  
227 typical solution form  $e^{\gamma t}$  with  $\gamma$  being a constant growth rate cannot be applied. Therefore, we seek  
228 solutions in the form of

$$w(x, t) = e^{ikx} \psi(z, t, \tau), \quad (5.2)$$

229 and we expand  $\psi(z, t, \tau) = \sum_m f_m^K(t) \varphi_m^K(z, \tau)$ . The  $\varphi_m^K(z, \tau)$  functions are the eigenvectors of the Sturm-  
230 Liouville problem

$$\frac{d^2 \varphi_m}{dz^2} - K^2 \varphi_m = - \frac{1}{D_m} K^2 n! S_n(z, \tau) \varphi_m, \quad \varphi_m(0, \tau) = \varphi_m(-H/z_0, \tau) = 0, \quad (5.3)$$

231 where  $D_m(K)$  is the corresponding eigenvalue, and normalized such that

$$\int_{-H/z_0}^{Z_0} K^2 n! S_n(z, \tau) \varphi_m^K(z, \tau) \varphi_l^K(z, \tau) dz = \delta_{ml} \quad (5.4)$$

232 with  $n = 1$  is for steady state radiation and  $n = 2$  for diurnal radiation. As we shall see, the eigenvalues  
233  $D_m$ 's control the growth of the perturbations in the inviscid limit.

234 A second simplification that we seek is to replace  $n! S_n(z, \tau)$  with its limiting value  $n! S_n(z, 0) = e^z$  in  
235 (5.1) and the attendant Sturm-Liouville problem. This assumption is justified by considering that, by  
236 the time the linear stage of perturbation growth comes to an end,  $\tau$  is still very small. Indeed, one way  
237 to interpret the Péclet number is to see it as the ratio of  $t_0$  (the time scale of growth of perturbations)  
238 to the diffusive time scale  $Z^2/k$ . Thus at large Péclet numbers the perturbations ought to experience a  
239 background state whose only mode of change is self-similar. In Appendix A we verify that the effect of  
240 the neglected surface boundary layer on the spectral properties of the Sturm-Liouville problem is small,  
241 especially on the eigenvalues  $D_m$ 's, which control how perturbations grow in time.

242 For a given  $K$ , there are countable eigenvalues  $D_1(K) > D_2(K) > \dots$ , and the corresponding  
243 eigenvectors form an orthonormal basis.  $D_1(K)$  as a function of the wavelength  $\lambda = 2\pi/K$  is shown  
244 in Figure 3a, with a few representative eigenvectors shown in figure 3b. Note how, as  $K$  increases, the  
245 region over which the eigenvector is non-negligible decreases. In fact, with a simple rescaling of the  
246 problem, it can be shown that the extent of the non-zero region decreases as  $1/K$ . Although it is not  
247 possible to give an analytic expression for the  $D_m$ 's, we have  $D_m(K) = O(K^2)$  for  $K \ll 1$ , whereas  
248  $D_m(K) = O(K^0)$  for  $K \gg 1$ . In particular, the fact that the eigenvalues saturate at large wave numbers  
249 will have significant consequences. For a given horizontal wavenumber  $K$ , substituting (5.2) into (5.1)  
250 yields a system of coupled ODEs for the amplitude functions  $f^K(t)$ . In Appendix B we show that when  
251 the Reynolds number is large (with fixed Prandtl number), to leading order the system decouples, so  
252 that each amplitude function  $f^K(t)$  evolves independently from the other. For a given  $f^K(t)$ , the  
253 growth rate is controlled by the eigenvalue  $D_m(K)$ . Because we are interested in the characteristics of  
254 the fastest growing perturbations, we focus on the case  $m = 1$ . From now on,  $D(K) = D_1(K)$  and

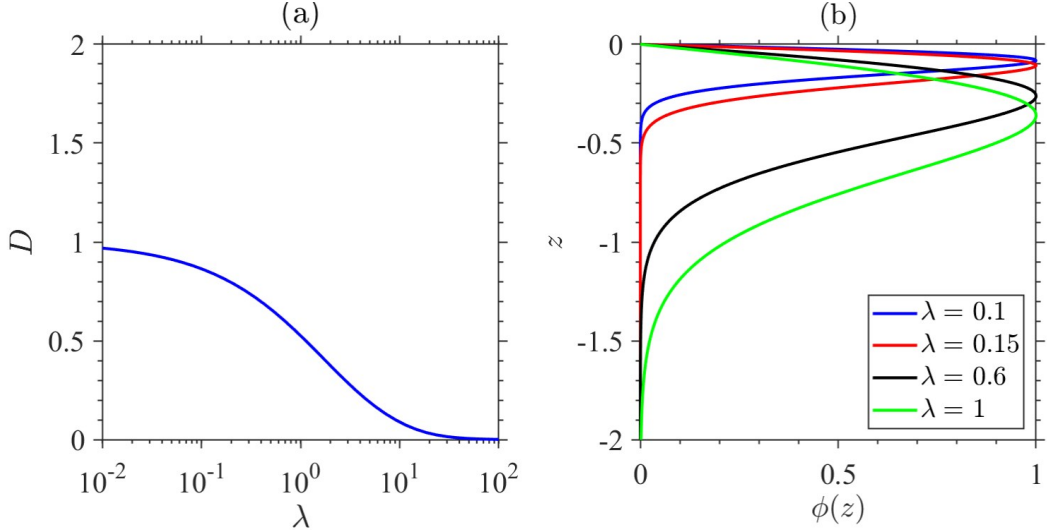


Figure 3: Solution of the Sturm-Liouville problem (5.3). (a) eigenvalue  $D$  as a function of  $\lambda$ . (b) eigenvector  $\phi(z)$  for the maximal  $D$  for a given  $\lambda$ . Solutions are obtained by solving (5.3) using a domain  $-5 \leq z \leq 0$ , boundary conditions  $\phi(-5) = \phi(0) = 0$ , and 1000 uniform grids. The eigenvalue  $D$  controls the growth rate in (5.8)-(5.9), (5.14), and (5.17), while the eigenvector  $\phi(z)$  represents the vertical structure of perturbations.

255  $f^K(t) = f_1^K(t)$ . By introducing the renormalized wavenumber  $K = K / \sqrt{D \text{Re}}$  to order  $O(\text{Re}^{-1/2})$  the  
256 amplitude  $f^K(t)$  satisfies the following equation

$$\frac{d^2 f^K}{dt^2} + K^2 \left( 1 + \frac{1}{Pr} \frac{dt}{dt} \right) \frac{df^K}{Pr r^{-1} K^4} - D(K) \frac{f^K}{n!} t^n = 0, \quad (5.5)$$

257 where  $Pr = Pe/\text{Re}$  is the Prandtl number of the fluid.

258 In the previous equation, we can discern two limits. In the limit  $K \rightarrow \infty$  with  $\text{Re}$  constant, (5.5) tends  
259 to a simple differential equation with constant coefficients, whose characteristic polynomial has roots

$$\sigma_{1,2}^\infty(K) = -K^2 \{1, Pr^{-1}\} \quad (5.6)$$

260 both of which are real and negative and thus exponentially damped. This is to be expected on physical 261 grounds, as for sufficiently small wavelengths diffusive effects will smooth out and eventually dampen 262 fluctuations. Conversely, when  $K \rightarrow 0$ , with  $K$  constant, the equation reduces to the modified Airy's 263 equation

$$\frac{d^2 f^0}{dt^2} - D(K) \frac{t^n}{n!} f^0 = 0, \quad (5.7)$$

264 whose solution grows asymptotically as

$$f^0(t) \approx \frac{1}{D(K)^{1/12} t^{1/4}} e^{(\sigma_d t)^{3/2}}, \quad \sigma_d = \frac{2}{3} D(K)^{1/3}, \quad \text{as } t \geq 1, \quad (5.8)$$

265 when  $n = 1$  and as

$$f^0(t) \approx \frac{e^{(\sigma_d t)^2}}{D(K)^{27/8} t^{1/2}}, \quad \sigma_d = \frac{D(K)^{1/4}}{2^{3/4}}, \quad \text{as } t \geq 1, \quad (5.9)$$

266 when  $n = 2$ . In practice, these asymptotic formulas apply already for  $t = O(1)$ , as seen by comparing 267 asymptotic solutions with the numerical integration of the corresponding equations (Figure 4). Note 268 that  $\sigma_d$  and  $\sigma_t$  tend to saturate as  $K \rightarrow \infty$ , whereas the viscous damping timescale becomes increasingly 269 shorter. On physical grounds, we can thus expect that at a certain wavenumber, dependent on the 270 Reynolds number, a cross-over occurs whereby viscous damping dominates and so very little energy 271 should be found above such wavenumber. To verify our intuition, we consider the general solution of 272 (5.5). It can be written in terms of special functions.

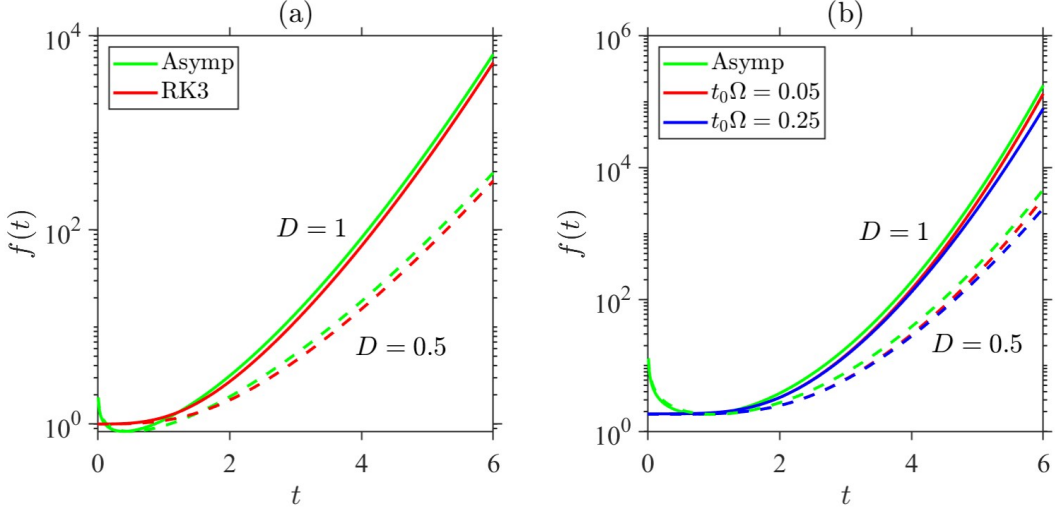


Figure 4: Comparison between asymptotic solution and numerical solution using a third-order Runge-Kutta method with  $dt = 0.01$ , and initial conditions  $f(0) = 1$  and  $f'(0) = 0$ . The comparison is to show asymptotic solution captures the growth of numerical solution as  $t \geq 1$ . Solid curves are for  $D = 1$ ; dashed for  $D = 0.5$ . (a) Asymptotic solution (5.8) and numerical solution of the modified Airy equation (5.7) with  $n = 1$ . (b) Asymptotic solution (5.9) and numerical solution of (5.7) with  $n = 2$ .

### 273 5.1. Time independent radiation

274 We consider first the case when  $n = 1$ . In this case we have

$$275 \quad f^K(t) = c_1(K)A(K, t) + c_2(K)B(K, t). \quad (5.10)$$

276 Here  $c_1(K)$  and  $c_2(K)$  are integration constants and the functions  $A$  and  $B$  can be expressed in terms of Airy's  $Ai$  and  $Bi$  functions

$$277 \quad A(K, t) = e^{\bar{\sigma}(K)t}Ai(\zeta(K, t)), \quad B(K, t) = e^{\bar{\sigma}(K)t}Bi(\zeta(K, t)), \quad \zeta(K, t) = \frac{(1 - Pr^{-1})^2 K^4 + 4D(K)t}{4D(K)^{2/3}}, \quad (5.11)$$

278 and  $\bar{\sigma}(K)$  is the arithmetic mean of the  $\sigma_i^\infty(K)$ 's. The integration coefficients are given by

$$279 \quad c_1(K) = \frac{(\bar{\sigma}(K) - 1)Bi(\zeta(K, 0))f'(0) + Bi'(\zeta(K, 0))f(0)}{\Delta(K)}, \quad (5.12)$$

280 and

$$281 \quad c_2(K) = -\frac{(\sigma(K) - 1)Ai(\zeta(K, 0))f'(0) - Ai'(\zeta(K, 0))f(0)}{\Delta(K)}, \quad (5.13)$$

282 with  $\Delta(K) = Ai(\zeta(K, 0))Bi'(\zeta(K, 0)) - Ai'(\zeta(K, 0))Bi(\zeta(K, 0))$ .

283 For  $t > 1$  the solution can be asymptotically expressed as

$$284 \quad f^K(t) \approx e^{\bar{\sigma}_t t} K^4 \left( \frac{Pr - 1}{Pr} \right)^{2/3} + 4Dt, \quad (5.14)$$

$$\Sigma_t = -\frac{K^2}{2} \frac{1 + Pr}{Pr} + \frac{1}{12Dt} K^4 \left( \frac{Pr - 1}{Pr} \right)^{2/3} + 4Dt - \frac{1}{12Dt} K^4 \left( \frac{Pr - 1}{Pr} \right)^{2/3}.$$

285 The solution when molecular viscosity and diffusivity are equal ( $Pr = 1$ ) is particularly illuminating, since in this case the solution is simply the inviscid solution multiplied by the viscous damping term.

$$286 \quad f^K(t) \approx \frac{1}{D(K)^{1/12} t^{1/4}} e^{-K^2 t + (\sigma_t t)^{3/2}}, \quad \sigma_t = \frac{2}{3} D(K)^{1/3}. \quad (5.15)$$

287 Neglecting the (weak) algebraic dependence on time of the prefactor, we see that evolution of a perturbation with a horizontal wavenumber  $K$  is controlled by the time- and wave-number-dependent

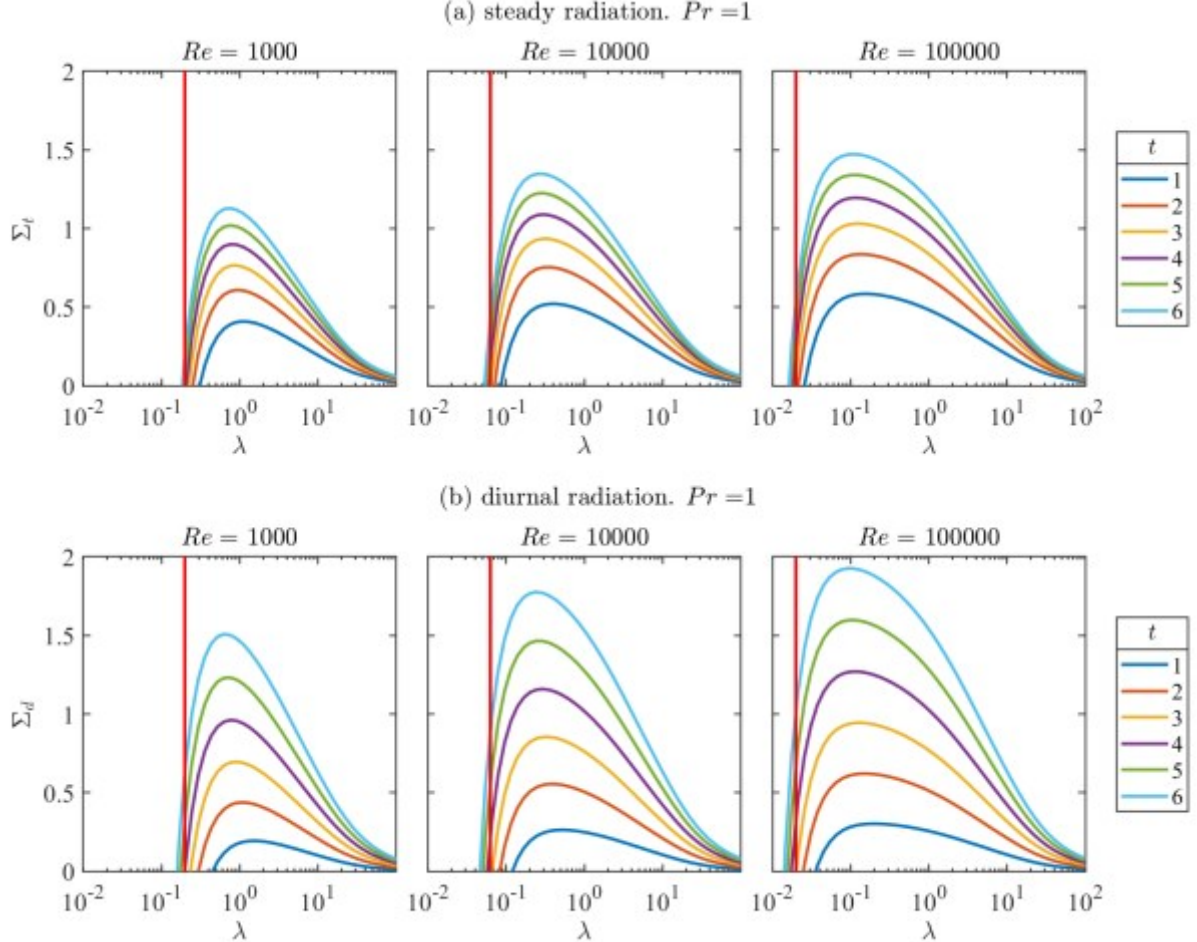


Figure 5: Asymptotic growth rate  $\Sigma$  vs wavelength at different times. The vertical red lines indicated the estimated high-frequency cutoff  $K = 1$ , i.e.  $\lambda / Re \approx 2\pi$ . (a) Steady radiation; (b) Diurnal radiation.

285 growth rate

$$\Sigma_t = \frac{1}{Re} - \frac{K^2}{D(K)} + \frac{\beta}{3} \frac{D(K)tRe^2}{D(K)tRe^2}. \quad (5.16)$$

286 Figure 5a shows the growth rate for a range of times as a function of the wavelength. Note that  $\Sigma_t$  is at  
287 most  $O(1)$ , which vindicates the choice of  $t_0$  as the relevant time scale for the process.

288 For a given  $Re$ , there is a Reynolds number dependent  $t_{\min}$  such that for  $t < t_{\min}$  the time-dependent  
289 growth rate  $\Sigma_t(K, t) < 0$ . This can be easily seen considering that as a function of  $K$  the viscous damping 290  
is a convex function which tends to a value  $O(1/Re)$  for  $K \rightarrow 0$ , whereas the inviscid growth is a concave 291  
function which approaches zero as  $K \rightarrow t$  for small values of  $K$  (figure 6).

292 To find how  $t_{\min}$  depends on  $Re$ , we consider the following ansatz  $t_{\min} = \beta Re^{-2}$ . When substituted  
293 into (5.16), the Reynolds number is factored out, leaving an equation for  $\beta$  that can be easily solved 294  
numerically. We obtain  $\beta \approx 491$  and a Reynolds-independent marginal wavelength  $\lambda_{\text{mar}} \approx 10.7$ . Past 295  
the range of wavelengths that experiences growth widens. The upper limit of the range increases as 296  $Re \propto t - t_{\min}$ . The lower limit of the range decreases as  $Re^{-1/2}(t - t_{\min})^{-1/4}$ . The peak of the growth rate 297 rapidly  
shifts to smaller wavelengths (figure 5a). The existence of a minimum time that needs to elapse 298 before  
instabilities can grow implies that instabilities will appear only after the background stratification 299  
has grown sufficiently. Since the non-dimensional time-dependent background stratification is  $N^2 = -te^z$ , 300  
the minimum near-surface background stratification necessary to sustain perturbations is  $-t_{\min}$ .

301 However, we recall that the superexponential growth given by (5.16) is not expected until  $t \gtrapprox 1$ . 302  
Therefore, for large values of the Reynolds number, by the time the solution enters the superexponential 303  
phase, a range of wavelengths is already poised to grow. Moreover, for large values of  $Re$ , the growth 304 rate  
for most wavelengths experiencing growth is only weakly dependent on the Reynolds number. Only

305 wavelengths that are close to either side of the interval see a significant departure from purely inviscid  
 306 growth. Thus, when comparing our results with numerical simulations, we use the inviscid limit.

307 The asymptotic expression is more complicated when  $Pr = 1$ , but as long as  $Pr$  remains finite, there  
 308 is no qualitative change in the behavior of the solution and little quantitative change. In fact, as we 309  
 shall see, the predicted growth rate and peak wavelength at  $Pr = 1$  match the values observed in the 310  
 numerical simulation at  $Pr = 10$ .

311 The above analysis suggests that instabilities will always appear, provided that enough time is allowed 312  
 for the stratification to reach its critical value, regardless of the magnitude of the Reynolds number. 313  
 However, as we remarked above, equation (5.5) was derived in the large  $Re$  limit. Superexponential growth 314  
 requires  $t_{\min}$  to be  $\gtrsim 1$  or larger. For values of  $Re$  greater than 20, by the time the superexponential 315  
 phase begins, there is already a range of wavelengths with positive growth rates. Whether values of  $Re$  316  
 smaller than 20 can still be considered "large" for the purpose of the theory remains to be seen. It is 317  
 certainly reasonable to assume that no matter how small the Reynolds number is, a sufficiently large 318  
 accumulation of negative buoyancy at the surface should be able to overcome the stabilising effect of 319  
 viscosity and diffusion, but this is a question that our theory cannot answer with certainty. Moreover, our 320  
 theory works in the small  $\tau$  limit. Under highly diffusive conditions, the growth of the surface boundary 321  
 layer cannot be neglected.

## 322 5.2. Diurnal solar radiation

323 For the diurnal radiation case ( $n = 2$ ), the general solution to (5.5) can be expressed in terms of a  
 324 combination of Hermite polynomials and hypergeometric functions, which play the role of Airy's functions 325  
 for the  $n = 1$  case. In this case, it is the hypergeometric function that dominates the behaviour for large 326  
 values of  $t$ . For large  $t$  the asymptotic solution is

$$f^K(t) \approx c_2(K) e^{\Sigma_d t} \left[ \frac{\sqrt{2Dt}}{K^4} \left( \frac{Pr-1}{Pr} \right)^2 + 2Dt^2 \right]^{\frac{K^4}{(32D)^{1/2}} \left( \frac{Pr-1}{Pr} \right)^2} ,$$

$$\Sigma_d = -\frac{K^2}{2} \frac{1+Pr}{Pr} + \frac{1}{4} \frac{K^4}{Pr} \frac{Pr-1}{Pr}^2 + 2Dt^2^{\frac{#_{1/2}}{#_{-1/4}}} , \quad (5.17)$$

327 where in this case  $c_2(K)$  is the coefficient of integration associated to the Hypergeometric function. The  
 328 growth rate  $\Sigma_d$  is dependent on time and wave number, which, when  $Pr = 1$  can be written as (Figure  
 329 5 b)

$$\Sigma_d = -\frac{K^2}{D(K)Re} + \frac{\sqrt{Dt}}{2^{\frac{#_{1/2}}{#_{-1/4}}}} . \quad (5.18)$$

330 Relative to the steady radiation case, the growth is more gradual at the onset, and steeper at later times,  
 331 but the pattern is otherwise very similar.

332 In this case as well the background stratification must grow beyond a  $Re$ -dependent critical threshold 333  
 for instabilities to grow. The analysis is very similar to the one done for the steady radiation case, with 334  
 the exception that now  $t_{\min} \gtrsim 42Re^{-1}$  has the same value for the marginal stability wavelength. The 335  
 upper limit of the unstable range increases as  $Re t$ , whereas the lower range decreases as  $(Re t)^{-1/2}$  336 (figure  
 5b).

## Viscous and inviscid nonlinear growth rates

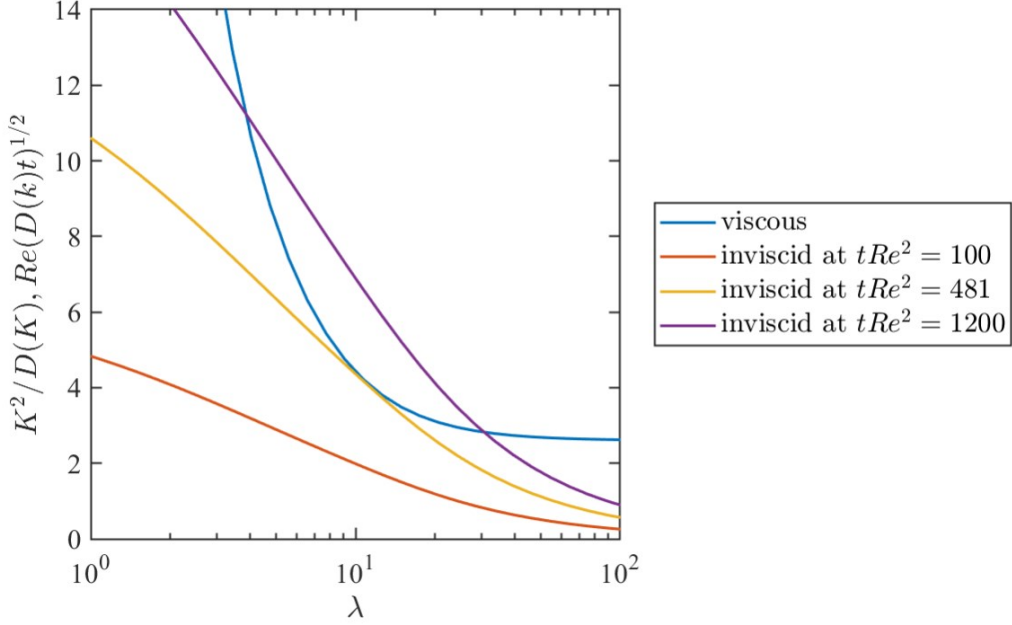


Figure 6: Viscous damping and inviscid growth rate as a function of wavelength under steady radiation conditions. The viscous damping is time independent, whereas the inviscid growth rate accelerates with time. Up to  $t \approx 481Re^{-2}$  viscous damping dominates. Past this time, a widening range of wavenumbers experiences net growth.

## 6. Comparison with numerical simulations

To validate the theory developed in the preceding section, we use the Stratified Ocean Model with Adaptive Refinement (SOMAR) to compare the prediction of our theory with the DNS simulations of RDC. SOMAR solves the Navier-Stokes equations under the Boussinesq approximation (Santilli and Scotti 2015; Chalamalla et al. 2017) using an operator splitting technique. The finite-volume discretization is second-order in space, while a third-order Runge-Kutta method is adopted for time marching. The Poisson equation is solved with an efficient multigrid solver. SOMAR adjusts the time step based on a CFL condition to maintain stability under advection. Viscous terms are treated implicitly.

We solve equations (2.1) and (2.2) in a rectangular domain extending from the surface to the bottom. Equations are discretised with uniform grids in each direction. The initial condition is a motionless, unstratified fluid plus perturbations of two types. The first type is initialised with single-mode perturbations with the most unstable wavelength predicted by (5.14) and (5.17) and the corresponding vertical structure shown in Figure 3b, with the peak normalised by  $W_0$  being 0.001. The second type is initialised with random temperature perturbations (normalised by  $T_0$ ) uniformly distributed in the range -0.01 to 0.01 over the entire domain. The boundary conditions are periodic in the horizontal direction. At the surface and at the bottom of the domain we use free-slip conditions and zero buoyancy flux. The use of free-slip conditions at the bottom removes the need to resolve the viscous sublayer. As convective activity is mostly confined with  $Z_0$ , the effect is negligible at large Reynolds numbers. The range of random temperature perturbations (-0.01 to 0.01) is chosen so that nonlinear terms are at least two orders of magnitudes smaller than linear terms. The effect of the magnitude of random perturbations is examined in Appendix D.

The configuration of all cases simulated and compared with the theory is described in Table 1. Cases TLR and THR consider time-independent radiation. The other two cases, DLR and DHR consider periodic radiation conditions. The non-dimensional parameters in the time periodic cases correspond to typical values found in Lake Onego (DLR) and Lake Michigan (DHR).

Together, these 4 cases cover a wide range of  $Re$  from 200 to 65000 with  $Pr = 10$ , which is typical for freshwater below the critical temperature. From our theory, we expect that over such a range of Reynolds numbers, the critical wavelength and vertical structure should vary appreciably. To capture these characteristics in each case, the choice of grid spacing is made with the following criteria in mind:

Case	Section	Re	Pe	$t_0\Omega$	$\delta/S$	D	$\lambda_p$	S	$N_h$	$N_v$
TLR	5.1.1	932	9323	—	0.009	0.64	0.6	1.2	166	122
THR	5.1.2	65444	654444	—	0.003	0.89	0.1	0.4	164	164
DLR	5.2.1	196	1959	0.09	0.013	0.51	1	1.7	161	173
DHR	5.2.2	20908	209080	0.26	0.004	0.83	0.15	0.5	163	205

Table 1: Configurations for the numerical simulations considered in sections 5.1 and 5.2. For each simulation, we list the Reynolds number  $Re = W_0 Z_0 / v$ , the Péclet number  $Pe = W_0 Z_0 / \kappa$ , the ratio  $\delta/S$  of the thickness of the viscous surface layer at  $\tau = 1/Pe$  to the thickness of the most unstable mode  $S$ , time scale ratio  $t_0\Omega$ , the eigenvalue of the most unstable mode  $D$ , the wavelength of the most unstable mode  $\lambda_p$ , the vertical extent (measured from the surface) of the most unstable mode  $S$ , the number of grid points  $N_h$  that resolve one horizontal wavelength, and the number of grid points  $N_v$  that resolve  $S$  in vertical. All lengths are measured in units of  $Z_0$ . In all the cases considered, the non-dimensional depth  $H$  of the domain is 5.

366 First, the vertical domain is 5 times  $Z_0$ , and horizontal domain is sized to contain 100 wavelengths with 367 the highest growth rate  $\lambda_p$ . Second, at least 161 horizontal grid points resolve the wavelength with the 368 highest growth rate  $\lambda_p$  and at least 40 grid points resolve the cutoff wavelength  $\lambda_{cut}$ . In the vertical 369 we use at least 122 grid points to resolve the sharp vertical variation  $S$  near the surface (see  $\lambda_p$ ,  $S$ , 370  $N_h$  and  $N_v$  in table 1). Third, and finally, in addition to the CFL condition necessary to ensure the 371 numerical stability of the scheme, the time step is further subject to the constraint that it should not 372 exceed  $t_0/40$ . These three rules ensure that the numerical setup does not bias the simulations. Sensitivity 373 to grid resolution tests are reported in Appendix C.

374 To distinguish between the linear stage (where our theory is expected to hold) and the non-linear 375 stage we compare  $\partial b/\partial t$  and  $w(\partial b/\partial z)$  in the buoyancy equation and  $\partial w/\partial t$  and  $w(\partial w/\partial z)$  in the 376 momentum equation. We compute the rms of each term for comparison. The average is taken over the 377 vertical range in which the eigenfunction of the most unstable wavelength varies ( $S$  in table 1 and figure 378 3b). The theoretical solution is normalised so that at  $t = 2$  it coincides with the numerical solution.

### 379 6.1. Time independent radiation

380 Case TLR initialized with single-mode perturbations is shown in figure 7a. The leftmost column 381 displays the time evolution of the horizontally averaged buoyancy. The red curve shows the value assumed 382 by the theory, while the blue dashed line is calculated from the SOMAR output. The two profiles are 383 still identical at  $t = 6$ , while significant difference exists at  $t = 7$ , signalling the end of the linear stage. 384 Even towards the end of the linear stage, the energy is still concentrated at the wavelength of the 385 initial condition (last column). Buoyancy and vertical velocity are shown in the central columns. The 386 perturbations evolve as a series of downward localized jets.

387 The growth of the perturbations in the simulation agrees well with the one predicted by the theory 388 until the magnitude of the nonlinear terms catches up with the magnitude of the linear terms around 389  $t = 6.7$  (figure 7b).

390 We estimate the time dependent growth rate from the simulation as

$$\Sigma_t \approx \frac{2}{3} \frac{d}{dt} (\ln \tilde{w}), \quad (6.1)$$

391 which compares extremely well with the theoretically predicted value (figure 7c) from  $t = 3$  to  $t = 6$ , 392 after which the former declines because the system approaches the nonlinear stage. The discrepancy at 393 earlier times may simply indicate that (6.1) is sensitive to small changes in  $w$ , since  $\partial w/\partial t$  and  $df^K(t)/dt$  394 agree well (figure 7b). Note that over the interval  $t = 2$  and  $t = 6$  the magnitude of the perturbation 395 grows by 3 orders of magnitudes.

396 Between  $0 < t < 1$ ,  $\partial w/\partial t$  drops slightly (figure 7b). Presumably, during this time, viscosity in (2.9) 397 and diffusivity in (2.10) play a role in the evolution of perturbations, because  $\partial \bar{b}/\partial z$  in (2.10), which grows

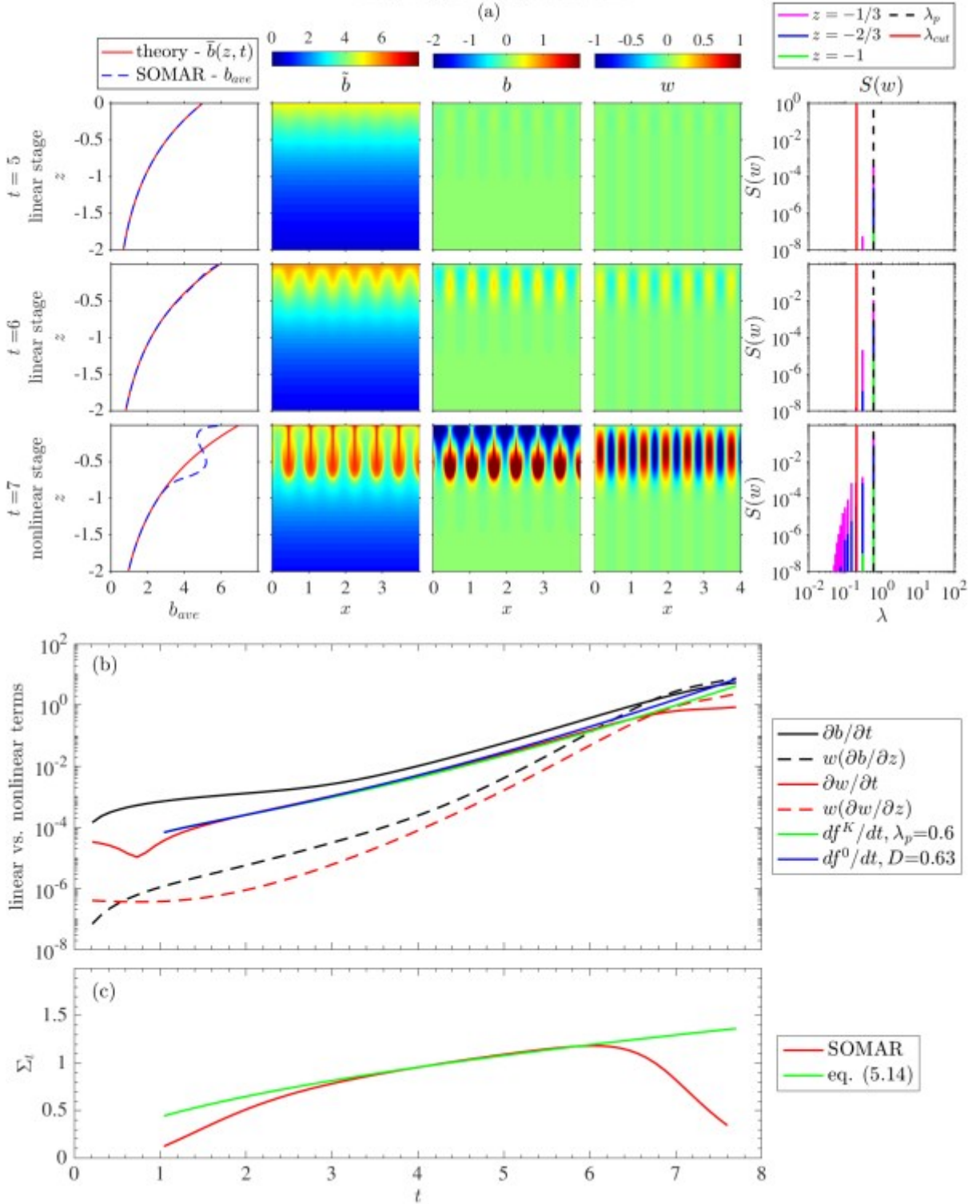


Figure 7: Evolution of RDC under time-independent radiation profile, with  $Re = 932$  and single-mode perturbations. (a) From rows 1-3, time advances. Column 1, comparison between theoretical basic state buoyancy  $\bar{b}(z, t)$  and horizontally averaged buoyancy profile  $b_{ave}$ . Column 2, side view of total buoyancy  $b$ . Column 3, side view of perturbation buoyancy  $b$ . Column 4, side view of vertical velocity, which is also perturbation vertical velocity  $w$ . Column 5, vertical velocity spectrum at  $z = -1, -2/3$ , and  $-1/3$ .  $\lambda$  is the wavelength of the perturbations.  $\lambda_p$  represents the theoretical most unstable wavelength.  $\lambda_{cut}$  the theoretical cutoff wavelength. Note the appearance of a spectral line at half the forcing wavelength due to the quadratic term in the equation of motion at  $t = 5$ . Only when the flow becomes fully nonlinear we observe energy at wavelengths smaller than  $\lambda_{cut}$ . (b) rms of linear and nonlinear terms in the legend and  $df^K(t)/dt$  and  $df^0(t)/dt$  as a function of time.  $\lambda_p$  is calculated from (5.14), and  $D$  is computed via (5.3). (c) growth rate as a function of time. The Red curve is computed from the SOMAR output. The green curve is the theoretical value (5.14).

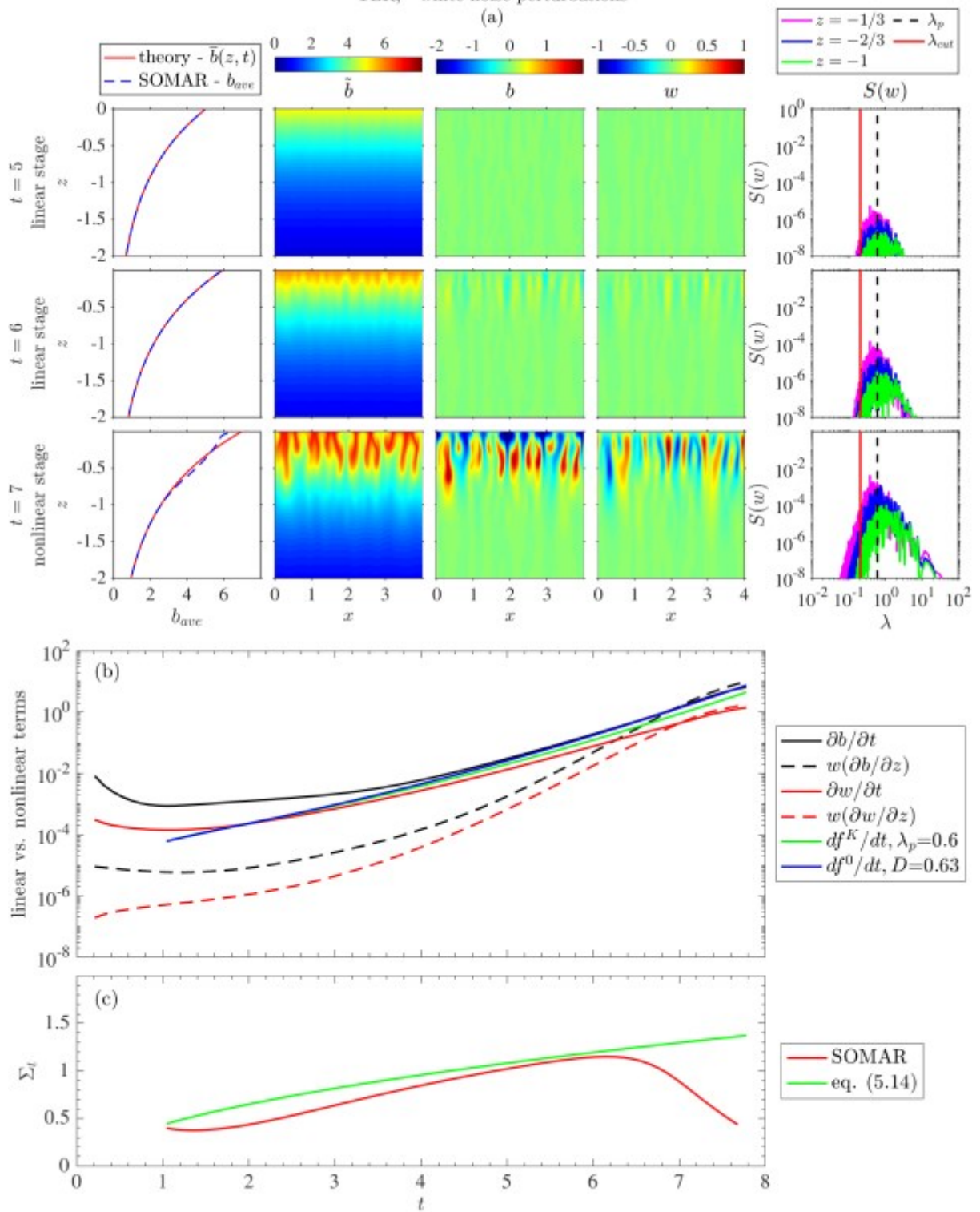


Figure 8: Same as figure 7 but with white-noise perturbations.

from 0, is not strong enough. This does not contradict the balance (4.1) and (4.2) and the subsequent analysis in sections 4 and 5. (4.1) and (4.2) target the evolution of perturbations when  $\partial b / \partial z$  grows continuously, and the analysis which follows applies for  $t > 1$ .

Simulations of case TLR with white-noise perturbations are shown in figure 8. The major difference in this case is that the spectrum contains energy over the range of wavelengths that experience positive growth, peaked on the wavelength of maximal growth ( $\lambda_p = 0.6$  at  $Re = 932$ ) predicted by the theory, which also predicts well the vertical envelope of the perturbations, with a peak at  $z = -0.25$  (figure 3b).

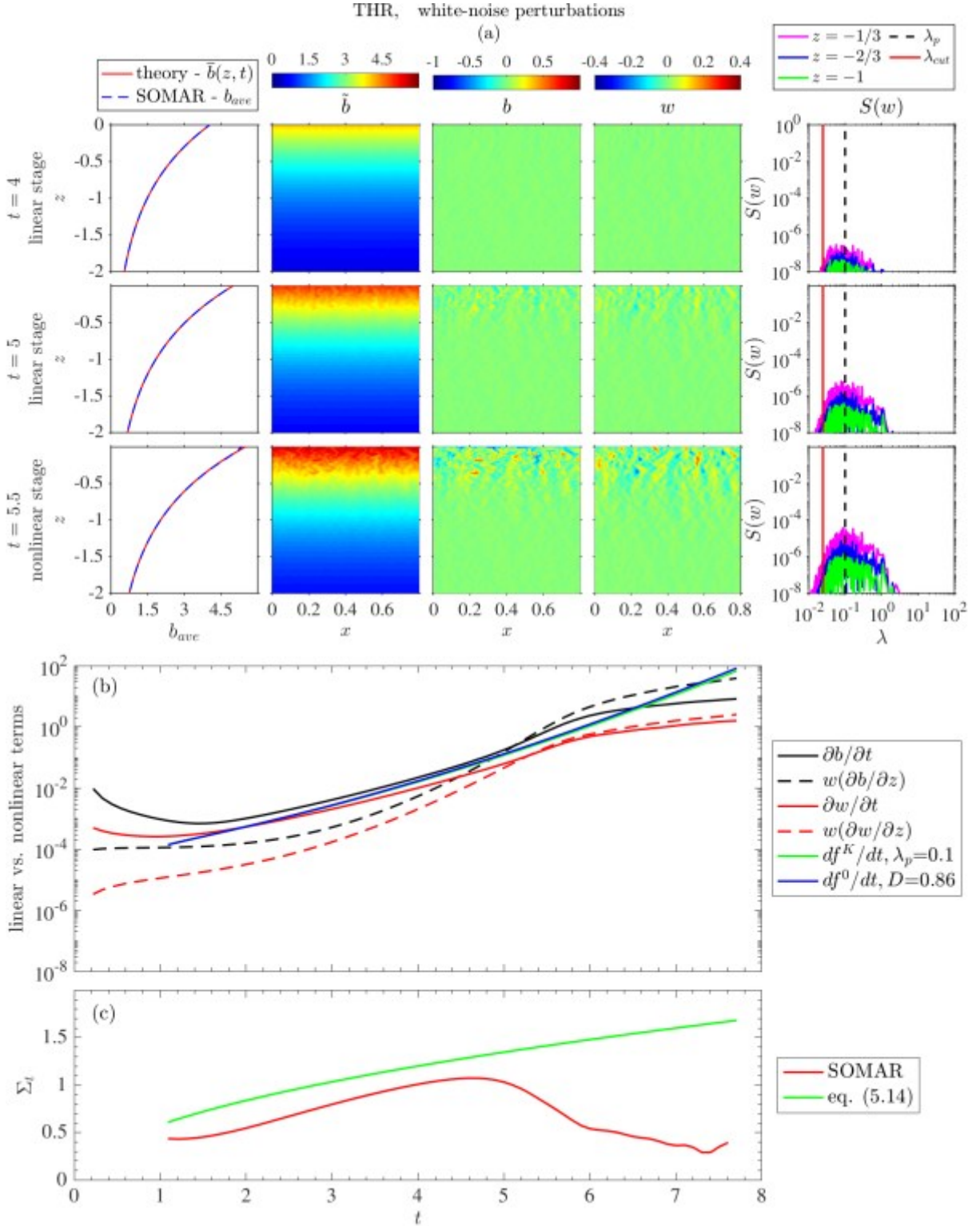


Figure 9: Same as figure 7, but with  $Re = 65444$ , white-noise perturbations and smaller colorbar range for columns 1-4.

405 Towards the end of the linear stage, there is a shift of the spectrum to larger wavelengths, likely due 406 to the nonlinear merger of plumes. Of course, in the nonlinear stage three dimensional effects become 407 dominant, which are not captured by our simulations. The spectra at different depths essentially overlap, 408 indicating strong coherence across the vertical dimension, consistent with a single mode being energized. 409

410 Overall, the theory predicts well how the perturbation grows in time, though the measured time- 410 dependent growth rate  $\Sigma_t$  is somewhat smaller than the one calculated from the theory, though the

411 latter is the growth rate expected from the most unstable mode, whereas in the simulation we have a 412 combination of modes across a range of horizontal wavenumbers that, while following the same growth 413 pattern, have different values of the eigenvalue  $D(K)$ . Thus it is to be expected that the measured  $\Sigma_t$  414 be lower than the theoretical value based on the most unstable wavelength.

415 Case THR considers a much larger value of the Reynolds number ( $Re = 65444$ ). In this case as well 416 the averaged numerical buoyancy profile agrees well with the profile used for the theoretical analysis up 417 to  $t = 5.5$ , after which the numerical solution becomes dominated by nonlinearity (figure 9a, column 1). 418 The spectra at different depths do not exactly overlap, as was the case at lower values of the Reynolds 419 number, though still peaking near the expected wavelength of maximal growth ( $\lambda_p = 0.1$ ). At large 420 values of the Reynolds number, the growth rate of higher vertical modal orders is less sensitive to the 421 modal number, and therefore we expect that the flow initialized with random perturbations will exhibit 422 a mixture of contribution from different modes. Overall, the theory captures well the growth of the 423 perturbations (figure 3b), though the presence of a continuum of energized wavelengths is reflected in 424 the overall time-dependent rate of growth, which, while following the expected increase in time between 425  $t = 2$  and  $t = 4.5$  is lower than the growth rate based on the most unstable wavelength and mode (figure 426 9c).

## 427 6.2. Diurnal solar radiation

428 Simulations forced by diurnal solar radiation with single-mode perturbations agree well with theory, 429 as was for case TLR in the preceding section. Therefore, in this section we focus on simulations with 430 white-noise perturbations.

431 Case DLR uses parameters typical of springtime conditions in a shallow temperate lake (Lake Onego, 432 Bouffard et al. (2019)). Compared to the other cases considered, diffusion effects are stronger, which 433 results in a relatively low value for the Reynolds number ( $Re = 196$ ). The agreement between the 434 buoyancy profile computed from the simulation and the one used in the theory is good up to  $t = 6$ , after 435 which nonlinearity dominates (first column in figure 10a; also figure 10b indicates that the nonlinearity 436 begins at  $t = 6.6$ ). The spectra at  $t = 5$  peak near  $\lambda \approx 1.2$ , close to the theoretical prediction  $\lambda_p = 1$ . 437 Beginning at  $t = 6$  we observe a shift of the energy to longer wavelength. This may be due to the flow 438 becoming more nonlinear. At  $\lambda_p = 1$  the corresponding mode-1 structure function (figure 3b), extends 439 to  $z = -1.7$ , with a peak at  $z = -0.4$ , which captures well the vertical envelope of the fluctuations. 440 The 441 growth of the rms fluctuations is well described by the theory (figure 10b). Over  $2 \leq t \leq 6.6$ , the 442 amplitude of the fluctuations increases by four orders of magnitude. Setting  $\tilde{w} = \exp(\sigma t^2)$  we compute 443 the growth 444 rate  $\Sigma_d = \sigma t$  as

$$\Sigma_d \approx \frac{1}{2} \frac{d}{dt} (\ln \tilde{w}). \quad (6.2)$$

443 The computed growth rate is in good agreement up to  $t = 6.2$  (figure 10c), after which the computed 444 growth rate declines as the linear and nonlinear terms become comparable (figure 10b). As it was for the 445 steady radiation cases, the calculated growth rate when the flow is initialized with a spectrally broad- 446 banded initial condition is somewhat lower than the theoretically predicted value. However, the trend in 447 time is very similar, and the same considerations that we presented in the steady radiation case apply 448 here as well. Overall, the agreement between theory and simulations is good.

449 Case DHR is representative of a deeper lake, close to critical temperature on a cloudy day. Such 450 conditions are often observed in Lake Michigan and Lake Superior (Cannon et al. 2019; Austin 2019). 451 With the role of viscosity and diffusivity diminished, the superexponential growth rate is larger, and 452 therefore the duration of the linear phase is shorter. Prior to  $t = 5$ , the theoretical basic state buoyancy 453 (4.6) and SOMAR output coincide, after which nonlinearity becomes apparent ( $t = 5.5$ ) (figure 11a, 454 column 1). The spectra peak around the theoretical wavelength of maximal growth ( $\lambda_p = 0.15$ ), which is 455 almost an order of magnitude shorter than in the previous case. The vertical envelope of the fluctuations 456 is 457 confined in the upper 10% of the water column during the linear phase, as expected from the mode-1 458 function associated to  $\lambda_p$ . The computed time-dependent growth rate follows the theoretical profile well, 459 though it is smaller than the value expected for the wavelength of maximal growth. Again, this is to 459 be expected, since the range of active wavenumbers is wide.

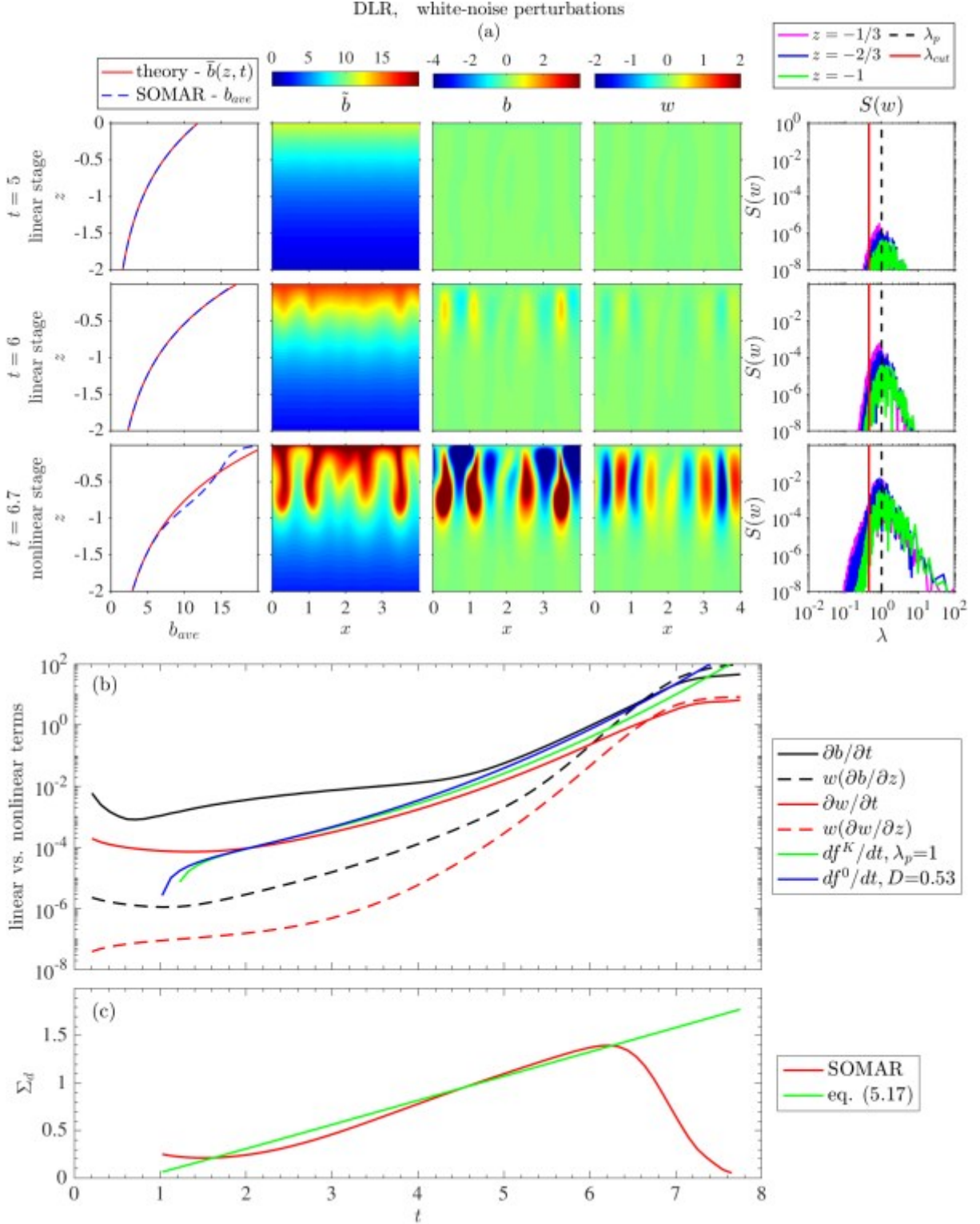


Figure 10: RDC under time-dependent radiation at  $Re = 196$  initialized with white-noise. Symbols and colors as in figure 7. Note that the colorbar range for columns 1-4 is greater.

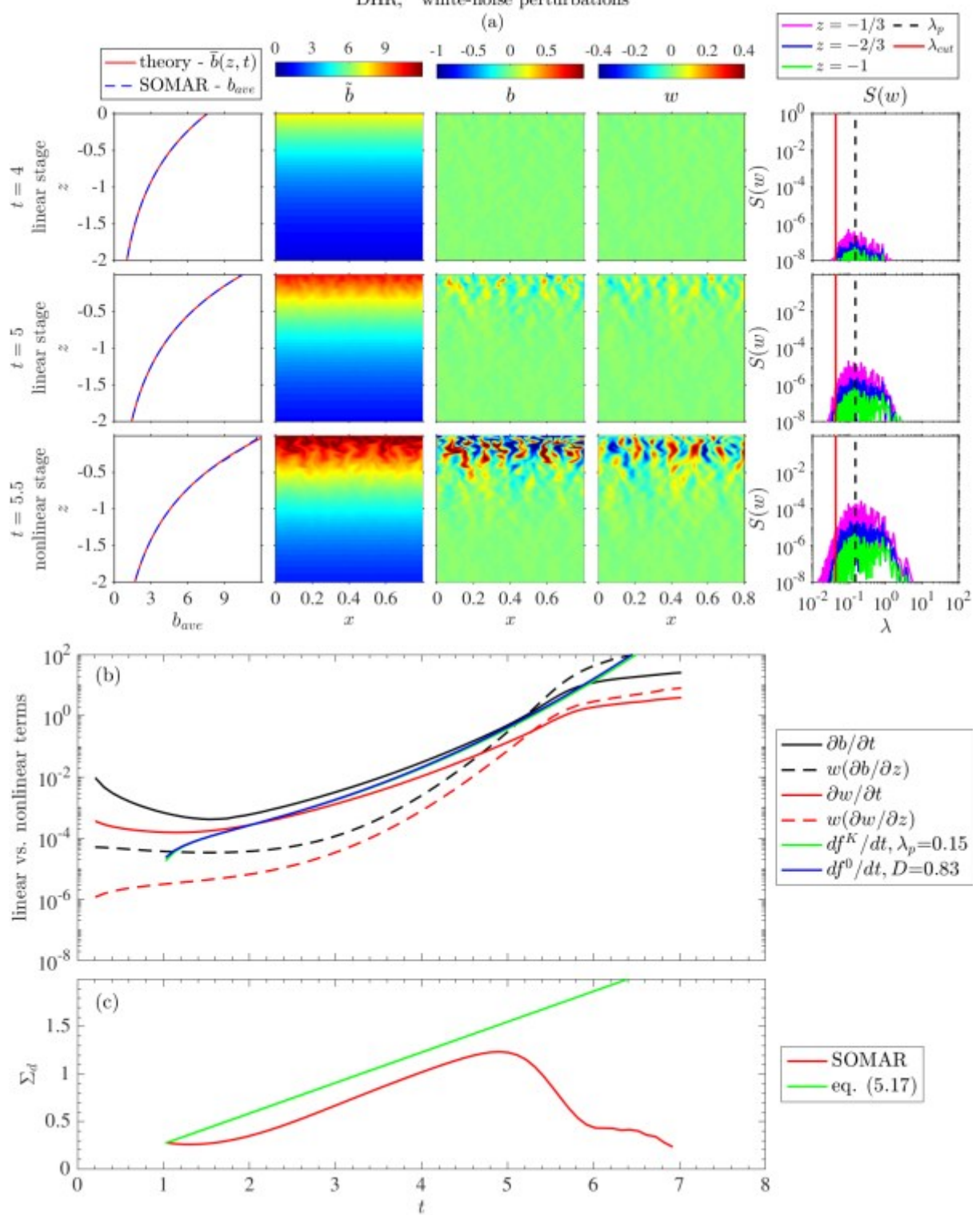


Figure 11: RDC under time-dependent radiation profile at  $Re = 20908$  with white-noise initial condition. Symbols and colors as in figure 7. Note that the colorbar range for columns 1-4 is smaller.

460 **7. Summary and conclusions**

461 We have considered the characteristics of the perturbations at the onset of Radiatively Driven  
 462 Convection. In this stage, the perturbations are small enough that it is permissible to linearise the  
 463 equations of motions around a quiescent background state characterised by a time-varying buoyancy  
 464 profile. We considered both steady radiation, which has been considered in recent laboratory experiments  
 465 (Bouillaut et al. 2019) and has applications to stellar interior (Kippenhahn et al. 1990), as well as time  
 466 dependent cases, more representative of Radiatively Driven Convection in temperate lakes during spring  
 467 time and which may have application to atmospheric convection (see, e.g. Figure 4 in Deardorff (1974)).  
 468 As opposed to the more traditional Rayleigh-Bénard convection, where the background state moves heat  
 469 at fixed rate from bottom to top boundary, while remaining constant in time, in Radiatively Driven  
 470 Convection the background state evolves in time, as heat is continuously added by radiation, and only  
 471 after the onset of convection heat can be effectively redistributed in the interior. By considering the most  
 472 likely balance in the dynamical equations, we build velocity and time scales which together with viscosity  
 473 allow the definition of a Reynolds number. We develop a theory that is valid for large values of the  
 474 Reynolds number that predicts the wavelength, vertical structure, and growth rate of the perturbations  
 475 during the initial linear stage. Due to the time-dependent nature of the background state, the growth of  
 476 perturbations not significantly affected by viscous damping has the form  $\exp[(\sigma t)^n]$  where the exponent is  
 477  $n = 3/2$  for time-independent radiation and  $n = 2$  for diurnal radiation. We have confirmed the analysis  
 478 by comparison with highly resolved DNS.

479 The theory gives a way to estimate the duration of the linear phase. Indeed, the latter terminates  
 480 when the amplitude of the nonlinear terms becomes comparable to the amplitude of the linear terms.  
 481 In Appendix D we show that the duration of the linear phase over a range of intensities of the residual  
 482 flow at dawn is found to be between  $3t_0$  and  $6t_0$ , where the linear time scale  $t_0$  is given by the last of  
 483 (4.8). For Lake Superior, assuming a water temperature of  $T = 3.5^\circ\text{C}$ , and a e-folding scale  $Z_0 = 10$ ,  
 484 we obtain  $t_0 \approx 80$  min on a cloudy day when the radiative intensity is  $S_0 \approx 200 \text{ W/m}^2$ . On a sunny day,  
 485 with the radiative intensity  $S_0 \approx 800 \text{ W/m}^2$ , the linear time scale is reduced to  $t_0 \approx 60$  min.

486 If we accept that once turbulence sets in the vertical gradient in temperature stabilises, the latter is  
 487 then set by the length of the linear phase. Ceteris paribus, a weaker initial circulation left over from the  
 488 previous cycle will result in a longer linear phase and thus a stronger stratification at the onset of the  
 489 turbulent phase, that is, a stronger temperature contrast upon which advection acts. This should result  
 490 in larger rms temperature fluctuations (relative to the background) during the day. With lakes as our  
 491 geophysical example of RDC under periodic radiation forcing, one way to test this prediction from an  
 492 observational point of view would be to correlate the strength of the fluctuations in temperature to the  
 493 strength of the residual circulation at first daylight.

494  
 495 **Acknowledgements** The authors wish to thank Prof. J. Austin, Prof. S. Llewellyn-Smith, Prof. J. 496  
 Bane, Prof. H. Seim, Prof. J. Rosman, Prof. S. Sarkar and Dr. T. Christopher for thoughtful comments.  
 497 The authors also thank three anonymous referees for providing constructive criticism.

498  
 499 **Funding** This work was supported by the National Science Foundation (grant number OCE-1829924).

500  
 501 **Declaration of interests** The authors report no conflict of interest.

502  
 503 **Author ORCID** Y. Chang, 0000-0002-1113-5870; A. Scotti, 0000-0001-8283-3070

## REFERENCE

504 J. A. Austin. Observations of radiatively driven convection in a deep lake. *Limnology and Oceanography*, 64(5):  
 505 2152–2160, 2019.

506 J. A. Austin, C. Hill, J. Fredrickson, G. Weber, and K. Weiss. Characterizing temporal and spatial scales of  
 507 radiatively driven convection in a deep, ice-free lake. *Limnology and Oceanography*, 2022.

508 S. Bogdanov, G. Zdorovennova, S. Volkov, R. Zdorovennov, N. Palshin, T. Efremova, A. Terzhevik, and 509  
 D. Bouffard. Structure and dynamics of convective mixing in lake onego under ice-covered conditions. 510  
 Inland waters, 9(2):177–192, 2019.

511 D. Bouffard, G. Zdorovennova, S. Bogdanov, T. Efremova, S. Lavanchy, N. Palshin, A. Terzhevik, L. R. Vinmå, 512  
 S. Volkov, A. Wüest, R. Zdorovennov, and H. N. Ulloa. Under-ice convection dynamics in a boreal lake. 513  
 Inland Waters, 9(2):142–161, 2019.

514 V. Bouillaut, S. Lepot, S. Aumaître, and B. Gallet. Transition to the ultimate regime in a radiatively driven  
 515 convection experiment. *Journal of Fluid Mechanics*, 861, 2019.

516 D. Cannon, C. Troy, Q. Liao, and H. Bootsma. Ice-free radiative convection drives spring mixing in a large lake.  
 517 *Geophysical Research Letters*, 46(12):6811–6820, 2019.

518 V. K. Chalamalla, E. Santilli, A. Scotti, M. Jalali, and S. Sarkar. Somar-les: A framework for multi-scale modeling  
 519 of turbulent stratified oceanic flows. *Ocean Modelling*, 120:101–119, 2017.

520 S. Chandrasekhar. Hydrodynamic and hydromagnetic stability. Oxford University Press., 1961.

521 T. Christopher, M. Le Bars, and S. G. L. Smith. Linear and nonlinear stability of rayleigh–bénard convection  
 522 with zero-mean modulated heat flux. *Journal of Fluid Mechanics*, 961:A1, 2023.

523 J. W. Deardorff. Convective velocity and temperature scales for the unstable planetary boundary layer and for  
 524 rayleigh convection. *J. atmos. Sci.*, 27(8):1211–1213, 1970.

525 J. W. Deardorff. Three-dimensional numerical study of the height and mean structure of a heated planetary  
 526 boundary layer. *Boundary-Layer Meteorology*, 7(1):81–106, 1974.

527 A. L. Forrest, B. E. Laval, R. Pieters, and D. S. Lim. Convectively driven transport in temperate lakes. *Limnology*  
 528 and *Oceanography*, 53(5part2):2321–2332, 2008.

529 R. Kippenhahn, A. Weigert, and A. Weiss. Stellar structure and evolution, volume 192. Springer, 1990.

530 D. Mironov and A. Y. Terzhevik. Spring convection in ice-covered freshwater lakes. IZVESTIIA-RUSSIAN 531  
 ACADEMY OF SCIENCES ATMOSPHERIC AND OCEANIC PHYSICS C/C OF IZVESTIIA- 532  
 ROSSIISKAIA AKADEMIIA NAUK FIZIKA ATMOSFERY I OKEANA, 36(5):627–634, 2000.

533 D. Mironov, S. Danilov, and D. Olbers. Large-eddy simulation of radiatively-driven convection in ice-covered lakes. 534  
 In Proceedings of the Sixth Workshop on Physical Processes in Natural Waters, pages 71–75. University of 535  
 Girona, 2001.

536 E. Santilli and A. Scotti. The stratified ocean model with adaptive refinement (somar). *Journal of Computational*  
 537 *Physics*, 291:60–81, 2015.

538 E. A. Spiegel. Convection in stars i. basic boussinesq convection. *Annual review of astronomy and astrophysics*,  
 539 9(1):323–352, 1971.

540 B. Yang, J. Young, L. Brown, and M. Wells. High-frequency observations of temperature and dissolved oxygen  
 541 reveal under-ice convection in a large lake. *Geophysical Research Letters*, 44(24):212–218, 2017.

## Appendix A

542 In this appendix we consider the Sturm-Liouville problem 5.3 subject to a more general profile for  
 543 the background stratification which includes the upper boundary layer. We compare three profiles: The 544  
 inviscid profile considered earlier, and two profiles in which the buoyancy gradient is (a) equal to zero 545  
 within the region  $-\tau \leq z \leq 0$ ; or (b) decreases linearly to zero within the same region. We discretise 546  
 the Sturm-Liouville problem with standard second-order differences. For the latter two cases, we resolve 547  
 the boundary layer with at least 20 points. Figure 12 compares the largest eigenvalue of the problem as 548  
 a function of wavelength: when  $\tau = 5 \times 10^{-3}$ , the eigenvalues computed with diffusive boundary layers 549  
 of type (a) or (b) are virtually indistinguishable. Compared to the inviscid profile, saturation at small 550  
 wavelengths occurs more slowly, but for the same wavelength the difference is never greater than 10%. 551  
 The difference is much smaller for  $\tau = 5 \times 10^{-4}$ . The corresponding eigenfunctions show little difference 552  
 between the two boundary layer cases. Relative to the eigenfunctions obtained from the inviscid profile, 553  
 we observe a slight shift downward of the peak in the eigenfunction when the boundary layer is included. 554  
 However, the difference is small. Since the focus of this paper is on the small  $\tau$  regime, this justifies the 555  
 use of the inviscid profile ( $\tau = 0$ ) in the calculations presented in the main paper.

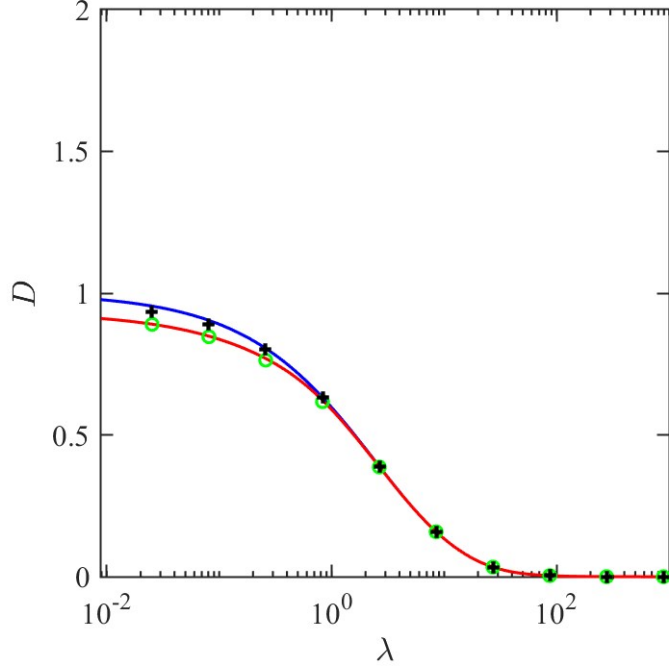


Figure 12:  $D$  as a function of  $\lambda$  for three different buoyancy profiles: inviscid profile (blue); profile with zero stratification in the boundary layer at  $\tau = 5 \times 10^{-3}$  (red) and  $\tau = 5 \times 10^{-4}$  (crosses); profile with stratification linearly approaching zero with the boundary layer at  $\tau = 5 \times 10^{-3}$  (circles).

## 557 Appendix B

558 In this appendix we present a more formal derivation of eq. (5.5). Let us consider a given  $K$  and let  $\mathbb{D}^2 \equiv (-K^2 + d^2/dz^2)$  and  $\mathbb{D}^2 \equiv -K^2$ . We substitute (5.2) into (5.1) and project over the eigenfunctions 559 obtained solving the Sturm-Liouville problem (5.3) to obtain a set of coupled ODEs for the functions 560  $f_m(t)$ . In particular, we need to consider integrals over the vertical domain  $\gamma = [-H/Z_0, 0]$  that can be 561 written as 562

$$I_{m n}^p = \int_{\gamma}^Z \mathbb{D}^p \varphi_m(z) \varphi_n(z) dz, \quad (7.1)$$

563 with  $p = 1, 2, 3$ . When  $p = 1$ , the integral reduces to

$$I_{m n}^1 = -\frac{\delta_{m n}}{D_m}, \quad (7.2)$$

564 where  $\delta_{m n}$  is the Kronecker's delta. When  $p = 2$ , we can use integration by part and the properties of 565 the eigenfunctions to obtain

$$I_{m n}^2 = \int_{\gamma}^Z \mathbb{D}^2 \varphi_m(z) \mathbb{D}^2 \varphi_n(z) dz = \frac{K^2}{D_m D_n} \delta_{m n} + \epsilon_{m n}^1, \quad (7.3)$$

566 with  $\epsilon_{m n}^p \equiv \int_{\gamma}^R (e^{pz} - 1) \varphi_m(z) \varphi_n(z) d\mu$ , where  $d\mu = K^2 e^z dz$  is the weighted measure of the interval. 567 Finally, again using integration by part

$$I_{m n}^3 = \frac{K^4}{D_m D_n} - \frac{\delta_{m n} + \epsilon_{m n}^2}{D_m} + \frac{\delta_{m n} + \epsilon_{m n}^1}{K^2} + \frac{\int_{\gamma}^R e^z \frac{d\varphi_m}{dz} \varphi_n d\mu}{K^2}. \quad (7.4)$$

568 The functions  $f_m(t)$  then must obey the following system of coupled ODEs:

$$\frac{d^2 f_m}{dt^2} + X \frac{D_m}{Re} f_m - 1 + \frac{1}{p_f} I_{m 1} \frac{df_1}{dt} - \frac{D_m}{Re p_f} I_{m 1} f_1 = -D_m \frac{t}{n!} f_m. \quad (7.5)$$

569 Introducing the rescaled wavenumber  $K = \sqrt{Re D_1}$ , we have

$$\frac{D_m}{Re} I_{m1}^2 = K^2 \frac{D_1}{D_1} (\delta_{m1} + \epsilon_{m1}^1), \quad (7.6)$$

570 and

$$\frac{D_m}{Re^2} I_{m1}^3 = -K^4 \frac{D_1^2}{D_m D_1} (\delta_{m1} + \epsilon_{m1}^2) + O(Re^{-1}). \quad (7.7)$$

571 Finally, we note that for finite values of  $K$  (i.e., small wavelengths) where viscous effects are going to be  
 572 important, the eigenfunctions are non-zero in a region whose size is  $O(Re^{-1/2})$  (see Figure 3(a)). Thus,  
 573 the coupling terms  $\epsilon_{m1}^i = O(Re^{-1/2})$  are negligible. Therefore, the (7.5) to  $O(Re^{-1/2})$  reduces to a set of  
 574 decoupled equations for the coefficients  $f_m$ 's, all of the form (5.5) with  $D = D_m$  and  $f = f_m$ . Since the  
 575 growth rate in the inviscid limit is proportional to the eigenvalue, we focus on the gravest mode ( $m = 1$ )  
 576 which, by definition, has the largest eigenvalue.

### 577 Appendix C Sensitivity to grid resolution

578 In this Appendix we show grid-independent tests. We choose THR and DLR for illustration because  
 579 they cover the maximal and minimum Reynolds numbers  $Re$  in this paper. As we can see from figures 13 580  
 and 14, as the grids are refined by a factor of 2 in both  $x$  and  $z$  directions, the growth rates are identical 581 in  
 the linear stage (before the growth rates drop). The only difference appears to be a slightly longer 582  
 duration of the linear phase.

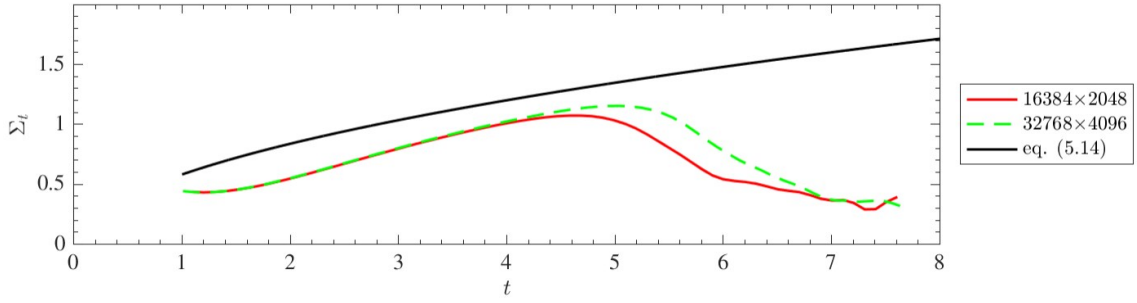


Figure 13: Growth rates as a function of time under steady radiation profile with  $Re = 65444$ . The resolution is indicated in the legend.

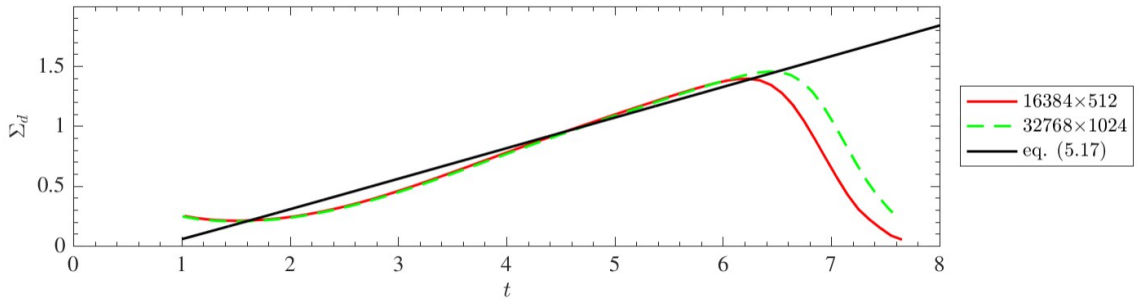


Figure 14: Growth rates under diurnal radiation profile with  $Re = 196$ . Symbols as in figure 13.

#### 583 Appendix D Effects of initial perturbation magnitude

584 This appendix examines the effect of the magnitude of the initial perturbations. Section 6 considers ran-585  
 dom temperature perturbations normalized by  $T_0$  uniformly distributed in the range from  $-10^{-2}$  to  $10^{-2}$ . 586  
 In this appendix, we compare different initial perturbation intensities  $(-10^{-1}, 10^{-1})$ ,  $(-10^{-2}, 10^{-2})$ , and 587  
 $(-10^{-3}, 10^{-3})$ . We choose cases THR and DLR to examine the perturbation effect because they cover 588  
 the largest and smallest Reynolds number  $Re$  considered in our numerical experiments. In both cases, 589  
 for the largest initial perturbations, the linear terms are less than an order of magnitude greater than 590  
 the nonlinear terms (upper panels in figures 15 and 16) and the system never experiences a linear stage. 591  
 In contrast, when the initial perturbations are smaller (last two cases), the growth rate is similar and for 592  
 the case with the smallest initial condition, the duration of the superexponential stage is indeed longer. 593  
 This results in the stratification at the onset of the nonlinear turbulent stage being stronger.

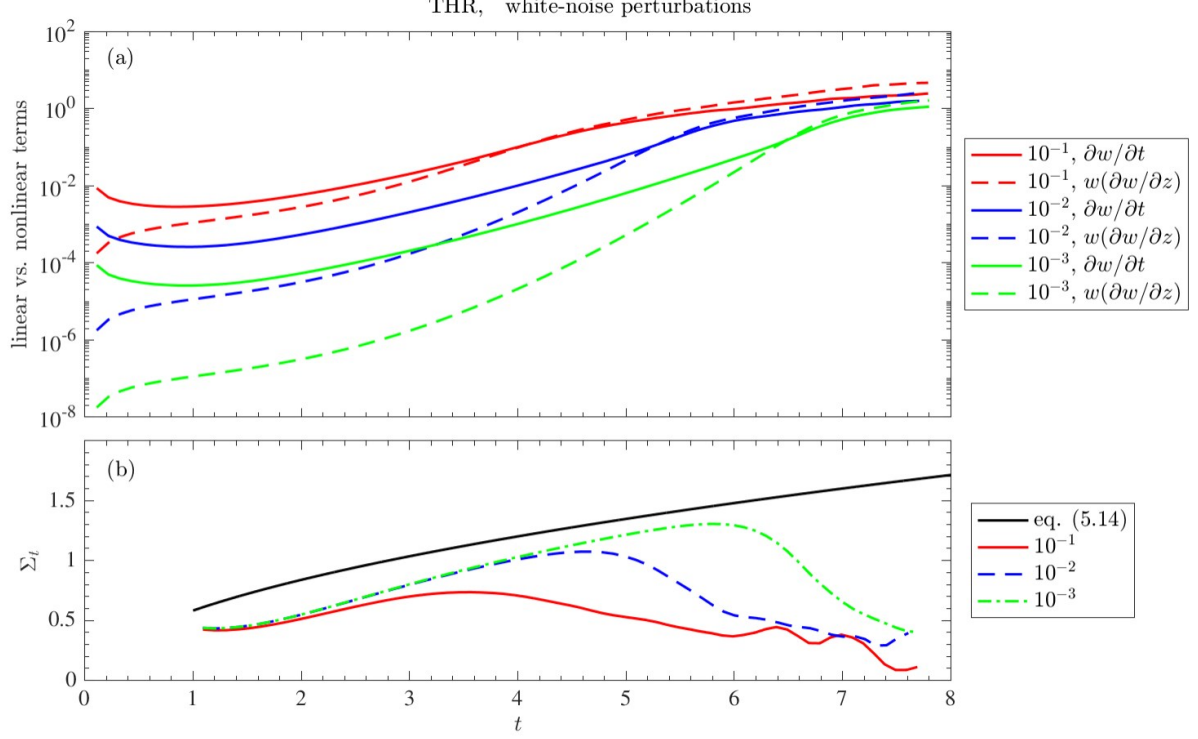


Figure 15: Evolution of RDC under time-independent radiation profile, with  $\text{Re} = 65444$ . (a) rms of linear and nonlinear terms. (b) growth rates. The numbers in the legend indicate the strength of the initial perturbations. Black curve is the theoretical value (5.14).

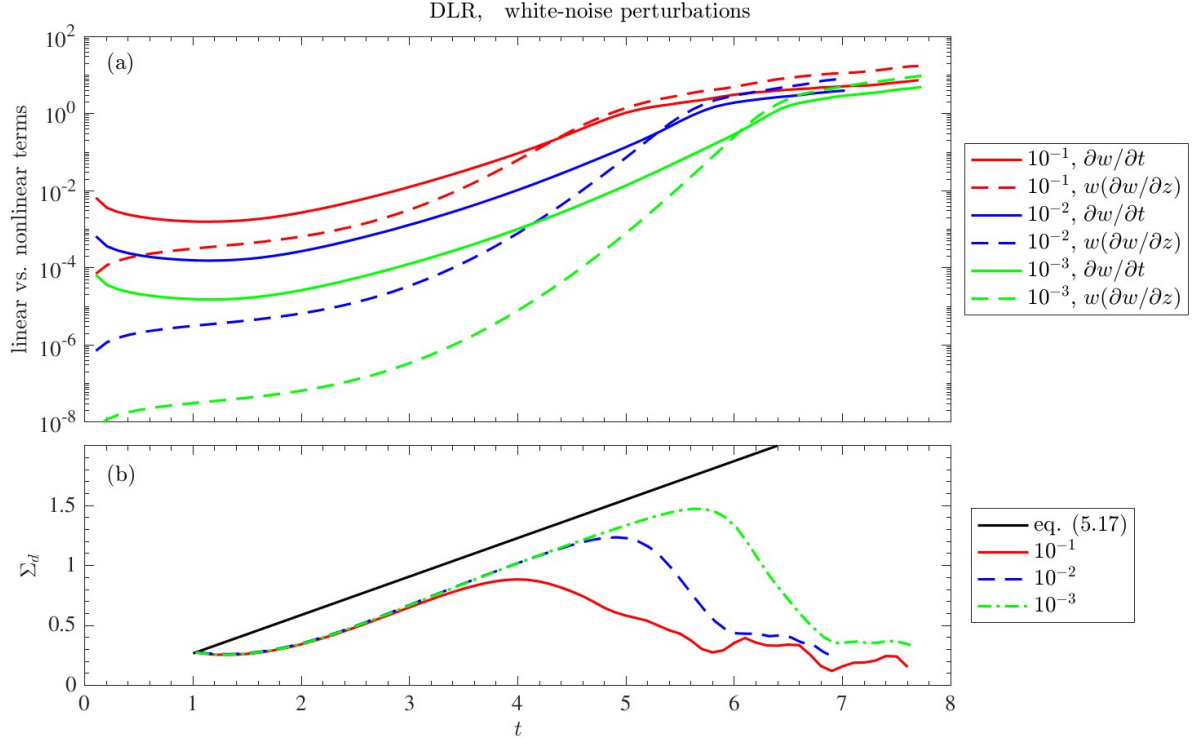


Figure 16: Same as figure 15, but under diurnal radiation profile and  $\text{Re} = 196$ .